The Pennsylvania State University

The Graduate School

Department of Electrical Engineering

PERFORMANCE EFFICIENCY OF THE WAVE-LARS SCANNING LIDAR SYSTEM

A Thesis in

Electrical Engineering

by

Brian K. Mathason

Submitted in Partial Fulfillment
of the requirements
for the Degree of

Master of Science

August 1994

We approve the thesis of Brian Mathason.

Date of Signature

_____ _____

Charles R. Philbrick
Professor of Electrical Engineering
Thesis Advisor

_____ _____

Timothy J. Kane
Assistant Professor of Electrical Engineering

_____ _____

lam-Choon Khoo
Professor of Electrical Engineering

_____ _____

Larry C. Burton
Professor of Electrical Engineering
Head of the Department of Electrical Engineering

Abstract

The performance efficiency of the WAVE-LARS (Water, Aerosol, Vapor Experiment - Lidar and Radar Sounder) scanning lidar instrument has been characterized and will be presented. WAVE-LARS (LARS) is an integrated remote sensing instrument developed by the Communications and Space Sciences Laboratory at the Pennsylvania State University for the purpose of atmospheric sounding. LARS consists of a three wavelength polarization Rayliegh/Raman scanning lidar, a millimeter wave scanning radar, and a static Rayliegh/Raman lidar. LARS measures the concentration, size, and shape of aerosols in the lower atmosphere. It is capable of volume scanning, providing 3-dimensional (3D) mapping of clouds and haze. With this instrument, the spatial and temporal dynamics of cloud formation can be measured.

The performance efficiency of each component of the scanning lidar system is evaluated. A total system efficiency is presented from the combination of the individual efficiencies and the coupling efficiencies between components. Sources of errors and deviations from the expected system performance are discussed. Modifications to the system for improved performance are suggested.

Table of Contents

List of Figures

List of Tables

Acknowledgments

Most of all I would like to thank my advisor, C. R. Philbrick for his guidance and support. The experiences and skills that I have accumulated under his counsel will be of value throughout my academic and professional careers. I would also like to thank my other committee members, I.C. Khoo and T. Kane for their support.

I would like to thank the many people who aided and supported me through the preparation of this thesis, Dan Lysak, Bob Smith, Mike O'Brien, George Evanisko, Jim Yurack, Paul Harris, Tim Stevens, Subha Maruvada, Sumati Rajan, Steve McKinley, Jim Anuskewicz, Anita Ventakaro, Glen Pancoast, Tom Petach. Each and every one of them has contributed to some part of this thesis.

The development and construction of the LARS system was made possible by funding by the Department of Energy, the Pennsylvania State University, and the National Science Foundation.

Finally I would like to thank the Applied Research Lab and the Mercury Seven Foundation for their financial support. Without their continued support I would not have been able to complete this thesis.

Chapter 1

Introduction

Measuring aerosol distributions in the boundary layer and troposphere is important for many reasons. Aerosols dominate the optical properties of the lower atmosphere and govern radiative transfer and visibility. Aerosols also play a significant role in the development of clouds and fog by acting as nucleation sites for condensation of water droplets. Because of their complex variability in space and time, aerosols are difficult to measure. A general description of the importance and the difficulty in measuring aerosols has been given by Carswell (1990).

Aerosols have been measured with various instruments and methods, in-situ and remotely. Airborne in-situ measurements are costly and are unable to provide vertical profile measurements. Radiosondes measure vertical profiles slowly and are subject to wind-directed horizontal drifting. Passive remote sensing systems provide range-integrated measurements instead of range-resolved measurements. Active remote sensing systems using lidar or radar offer advantages over these other instruments for measuring aerosol distribution because they are capable of producing range-resolved measurements with high spatial and temporal resolution.

The first measurements of atmospheric aerosols using laser remote sensing techniques were performed by Fiocco and Smullin (1963). They observed aerosols in the upper atmosphere with 10 km resolution. Since then, with the development of high-power pulsed lasers, along with high speed electronics and computers for data collection and processing,

laser remote sensing has become a significant tool for measuring aerosols. Significant aerosol measurements using lidar instruments have been demonstrated by Philbrick (1993), She (1992), Spinhirne (1980), and others (Clark and Whitby 1967; Rajan et al. 1993; Sassen 1991; Shipley et al. 1983).

1.1 Lidar Principles

Lidar (light detecting and ranging) is a technique for remote sensing of the atmosphere that is similar to radar remote sensing. An optical beam, typically from a laser, is emitted into the atmosphere; some of the photons are backscattered through interactions with molecules and particles in the atmosphere and are collected by the lidar receiver system as an optical signal. From the number of photons collected by the lidar receiver, information about the type, concentration, size, shape, and temperature of particles in the atmosphere can be inferred. Range, or altitude, information is obtained by using a pulsed emission source and time-gating the received optical signal.

1.2 Relevant Scattering Processes

There are many different interactions that can occur when radiation is incident upon matter, but of primary importance to the WAVE-LARS system are Rayleigh scattering, Mie scattering, and Raman scattering. It is also useful to look at the changes in the polarization of the light caused by interactions with the atmospheric constituents.

1.2.1 Molecular Rayleigh Scattering

Molecular scattering is an elastic process that occurs when the size of the scatterer is smaller than the wavelength of the incident radiation. The electric-field of the incident radiation induces a dipole moment in the molecule or atom which then re-radiates as a dipole field into 4π steradians. The scattering cross section has a λ^{-4} dependence, thus we expect to have the best sensitivity in the blue or ultraviolet region of the spectrum.

1.2.2 Mie Scattering

Mie Scattering is an elastic process that occurs when the size of the scatterer is comparable to or larger than the wavelength of the incident radiation. The scattering cross section is dependent upon the size and shape of the scatterer. The scattering size parameter is defined as $x = (2\pi a)/\lambda$, where a is the primary dimension of the scatterer, and λ is illuminating wavelength. As the relative size of the scatterer increases (x increases), there is an increased forward scattering component, and the scattering cross section becomes a complicated angular modal pattern. The wavelength dependence decreases with the relative size of the scatterer. For very large particles, such as cloud droplets, scattering is independent of wavelength. Aerosol scattering follows approximately a λ^{-1} dependence for wavelengths in the range of 0.2-10 μm region for smaller particles, like those found in low altitude clouds or haze. Mie scattering is a strong interaction which typically results in a backscattered intensity that is larger than the molecular scattering.

Figure 1.1 shows backscattering efficiency with respect to size parameter for two of the optical channels. Since the ratio varies with particle size, semi-quantitative information

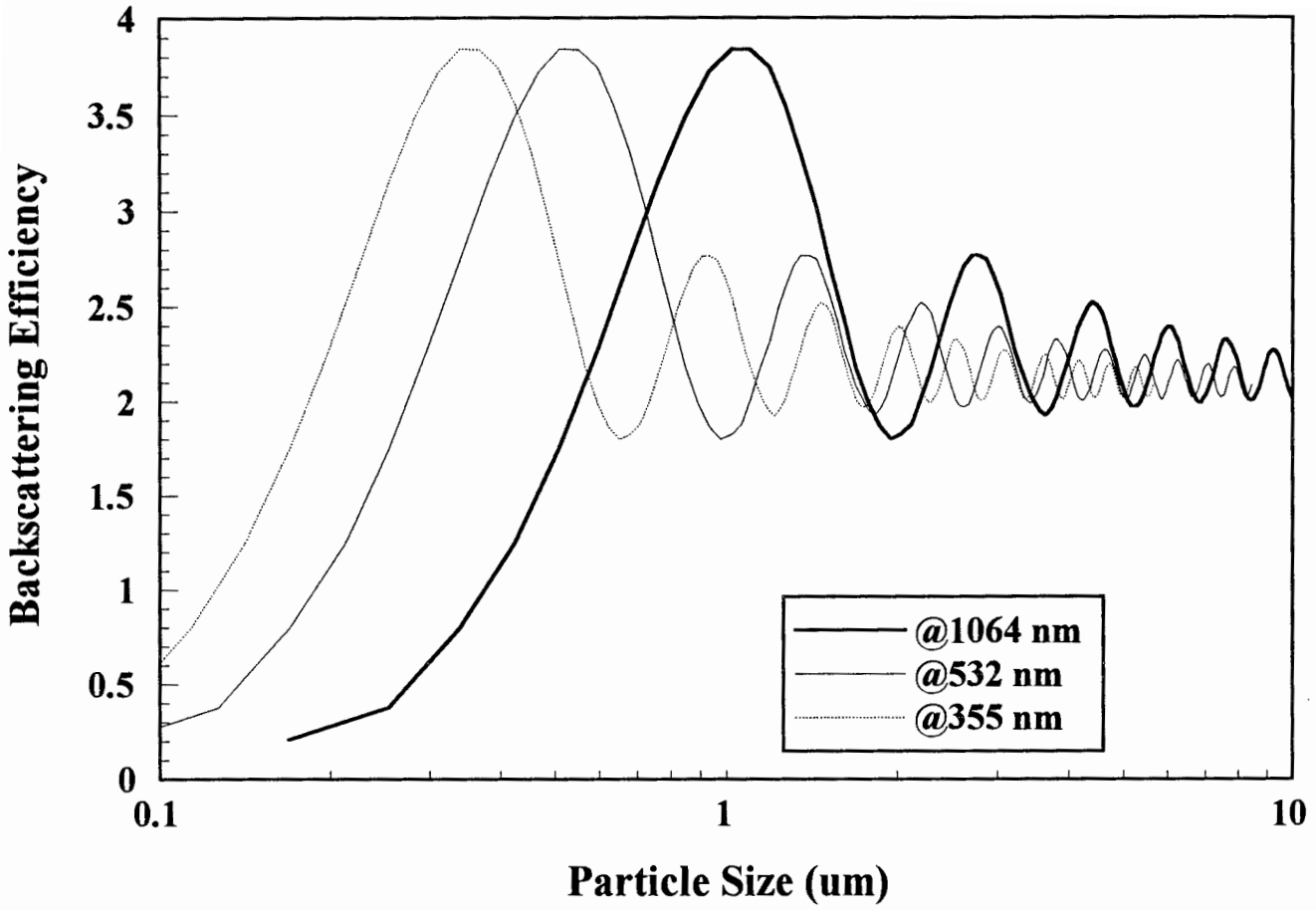

Figure 1.1. Wavelength dependence of the backscattering efficiency for aerosol particulates (data generated with program by Bohren and Huffman,1983, pp. 477-481)

about particle size distribution can be obtained. With the addition of two more wavelengths, even more detail about particle size distribution can be measured.

1.2.3 Raman Scattering

Raman scattering is an inelastic process where the scattering signal is frequency shifted due to the vibrational or rotational energy states of the molecules. Because the vibrational energy shift is different for each type of molecule or atom, Raman scattering can be used to sense specific constituents of the atmosphere (i.e. water vapor). This is a weaker interaction than Rayleigh scattering, with a cross section that is typically three orders of magnitude smaller. We are particularly interested in the Raman N_2 signal because it provides a direct measurement of extinction, and thus can be used to infer forward scatter relative to backscatter.

1.2.4 Depolarization

The polarization of linearly polarized incident light can be changed by many scattering processes, including molecular Rayleigh scattering from molecules with anisotropic polarizabilities, Mie scattering and multiple scattering. A useful parameter for measuring the change in polarization is the depolarization ratio. The depolarization ratio is given by

$$\delta_p \equiv \frac{I_s^{\perp}}{I_s^{\parallel}} \tag{1.1}$$

where $I_s^{\perp}$ and $I_s^{\parallel}$ are the intensities of the perpendicular and parallel scattered light with respect to the plane of polarization of the incident linearly polarized light beam. A review and assessment of the use of polarization lidar for studying clouds has been given by Sassen (1991).

1.3 The Lidar Equation

The lidar equation is used to characterize the expected return signal for a given lidar system. This equation is found in many different forms depending on the use. Equation 1.2 shows the lidar equation for a pulsed Rayleigh-Raman lidar system assuming single-scattering. This form of the equation (Harris, 1992) is particularly useful for understanding the effects of system efficiencies.

$$N(R) = \frac{E_L}{hc/\lambda_L} \times T(\lambda_L,R)\,T(\lambda_S,R) \times \frac{\sigma(\lambda_L,\lambda_S)\,n(R)\,\Delta R}{4\pi} \times \frac{\xi(R)A_o}{R^2} \times \eta_{eff}(\lambda_S) \qquad \textbf{(1.2)}$$

(1) (2) (3) (4) (5) (6)

where,

(1) number of scattered photons collected,

(2) number of laser photons transmitted,

(3) atmospheric transmission at the transmitted and received wavelengths integrated along the path from the attenuation coefficients,

(4) scattering probability in the integrated scattering volume,

(5) probability of reception from the scattering volume,

(6) optical efficiencies of the lidar detector and data system,

and,

$N(R)$ = number of photons returning from range (altitude) R,

E_L = laser pulse energy,

h = Planck's constant,

c = speed of light,

λ_L = emitted laser wavelength,

λ_S = scattered wavelength,

$T(\lambda_L,R)$ = atmospheric transmission along emitted path,

$T(\lambda_S,R)$ = atmospheric transmission along return path,

$\sigma(\lambda_L,\lambda_S)/4\pi$ = backscattering cross section for incident wavelength and scattered wavelength,

$n(R)$ = atmospheric number density at range R,

ΔR = integration range,

$\xi(R)$ = probability that light scattered from range R will reach the detector,

A_o / R^2 = acceptance solid angle of the receiver optics (A_o = area of receiving telescope)

$\eta_{eff}(\lambda_S)$ = efficiency of the lidar system

1.4 The WAVE-LARS System

The WAVE-LARS (Water, Aerosol, Vapor Experiment - Lidar and Radar Sounder) system, which I will refer to as LARS, was designed and constructed at Penn State's Communications & Space Science Laboratory. The design was based on LAMP, a

Rayleigh/Raman lidar system previous built and currently operated by the lidar group. Preliminary testing of LARS began in the summer of 1994.

LARS was designed to provide a more complete understanding of aerosols and clouds in the lower atmosphere by integrating multiple measurement channels. Semi-quantitative information about the size distribution and shape of aerosols is derived from measuring the backscattered signal at four wavelengths (ultra-violet, visible, infrared, millimeter) for the two orthogonal polarizations. A Raman nitrogen channel is used to account for molecular scattering in the aerosol Rayleigh channels and measures the extinction. LARS indirectly provides information about cloud formation since aerosols act as nucleation sites for water droplet condensation. Since clouds have a significant impact on radiative transfer in the atmosphere, looking at the temporal and spatial formation of clouds will provide valuable information for modelling of the atmosphere.

LARS actually consists of three separate remote sensing systems. It is the combination and comparison of data from these three systems that makes LARS a unique and powerful system. The three systems are the scanning lidar sounder, scanning radar sounder, and the static lidar sounder. All three systems are described in the following sections.

1.4.1 The Scanning Lidar Sounder

The scanning lidar sounder is illustrated in Figure 1.2. This system uses an Nd:YAG laser transmitting at 1064 nm, 532 nm, and 355 nm. The receiver/detector system has seven channels for the data signals. Channels for two orthogonal polarizations for each of the three transmitted wavelengths accounts for six of the channels. The extra channel is for measuring

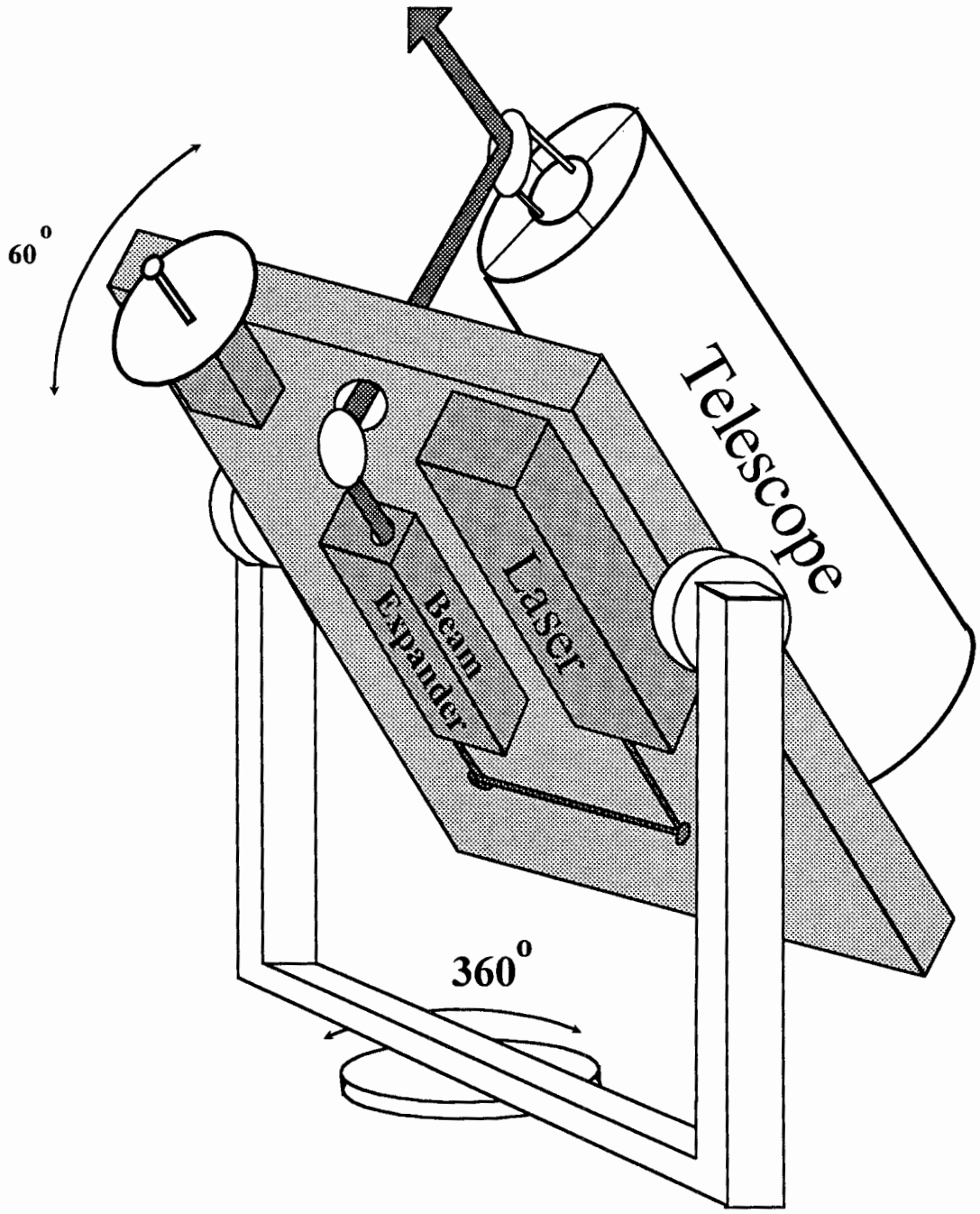

Figure 1.2. LARS Scanning System (illustrated by George Evanisko)

nitrogen concentrations for true extinction measurements. There is also the capability of adding one more channel in the future if desired.

The scanning lidar is the most sophisticated and the most versatile of the three LARS systems. In order to produce the most accurate measurements over the largest range, it is necessary to characterize the efficiency of the system. The primary focus of this thesis is quantifying the performance efficiency of the scanning system. Evaluating the efficiency of each component in the system allows us to predict sensing limitations, compensate for system errors, and identify weak points that can be improved in future enhancements to the system.

The scanning lidar system consists of six sub-systems; the scan control system, transmitter system, receiver system, detector system, data-acquisition and processing system, and safety system. A brief description of each sub-system follows. Several of the sub-systems critical to performance efficiency are discussed in more detail in following chapters.

Scan Control System

The transmitter/receiver systems are mounted on an optical table between the two forks of the scanning platform. This table has the capability of rotating around its center axis, and the whole fork rotates around its base. A dedicated computer drives stepper motors that provide the table rotations. The computer and motor controllers are programmed to perform several different scans including a cross-wind scan and a raster scan. Encoders in the motors warn the motor controllers if the motors stall or the system does not perform as expected for any reason.

Transmitter System

The transmitter is an Nd:YAG laser with a fundamental wavelength of 1064 nm. The linearly polarized beam is passed through harmonic-generating crystals to convert some of the energy to 532 nm and 355 nm. The laser beam is folded by two mirrors to align it with the center of the field of view of the receiver telescope. The beam is also passed through a beam expander to decrease the energy density (so that it becomes eye safe at a shorter range) and decrease divergence.

Receiver System

The main component of the receiver systems is a 16" diameter, f/7.8 Ritchey-Cretian telescope. The collected light is collimated by a system of lenses and passed through a Glan-Air prism polarizer to separate the orthogonal polarizations. Each of the polarization components is coupled into separate multimode optical fibers. The fiber positions are automatically corrected by stepper motors for optimal coupling. The light is guided by the fibers into two separate but similar detector systems located inside the field laboratory.

1.4.2 The Scanning Radar Sounder

The scanning radar sounder uses a 94 Ghz radar transmitter. The operating frequency was selected for a window in the atmospheric absorption spectrum and for Rayleigh scattering from particles on the scale of cloud droplet sizes. The large difference in transmission wavelength compared with that of the lidar takes advantage of the backscattering coefficient's wavelength dependence. Because of its lower attenuation in clouds, the radar sounder is able

to measure through thick clouds and multiple cloud layers that the lidar is not capable of penetrating.

The sub-system arrangement is similar to the scanning lidar system. Normally both scanning systems will be synchronized so that they are taking measurements of the same atmospheric volume.

1.4.3. The Static Lidar Sounder

The static lidar sounder will be used to measure water vapor at the zenith in conjunction with the scanning radar and lidar sounders. Measuring water vapor concentrations in conjunction with aerosol measurements provides a more complete picture of cloud formation. The Penn State LAMP lidar system (Harris, 1992) will be used for water vapor measurements until a separate static lidar is completed. The water vapor measurements can be added to the extra channel of LARS in the future. The LAMP measurements are constrained to a meridian plane at the present time.

Chapter 2

Transmitter System Efficiency

2.1 Transmitter System

A schematic illustration of the transmitter system of the scanning lidar system is shown in Figure 2.1. The laser is a commercially manufactured Nd:YAG laser emitting linearly polarized light at a primary wavelength of 1064 nm. Second and third harmonic wavelengths of 532 nm and 355 nm are generated from the primary wavelength using non-linear crystals. Specifications for the laser are listed in Table 2.1.

Table 2.1. Continuum Surelite II-20 Nd:YAG Laser

Pulse Energy	Maximum	Operating
@ 1064 nm	500 mJ	100 mJ
@ 532 nm	225 mJ	85 mJ
@ 355 nm	90 mJ	90 mJ
Pulse Width	4-7 ns	
Repetition Rate	20 Hz	
Divergence	0.6 mrad	(0.12 mrad)*
Beam Diameter	7 mm	(35 mm)*

* values in parentheses are beam properties after passing through the 5x beam expander.

The laser was chosen for its ruggedness and stability. Since the laser will be on the scanning table, it must be able to withstand shock and vibration.

The laser beam is reflected by two 2" diameter laser hard coated mirrors to steer it into the beam expander. The beam expander is an off-axis parabaloid that expands the beam

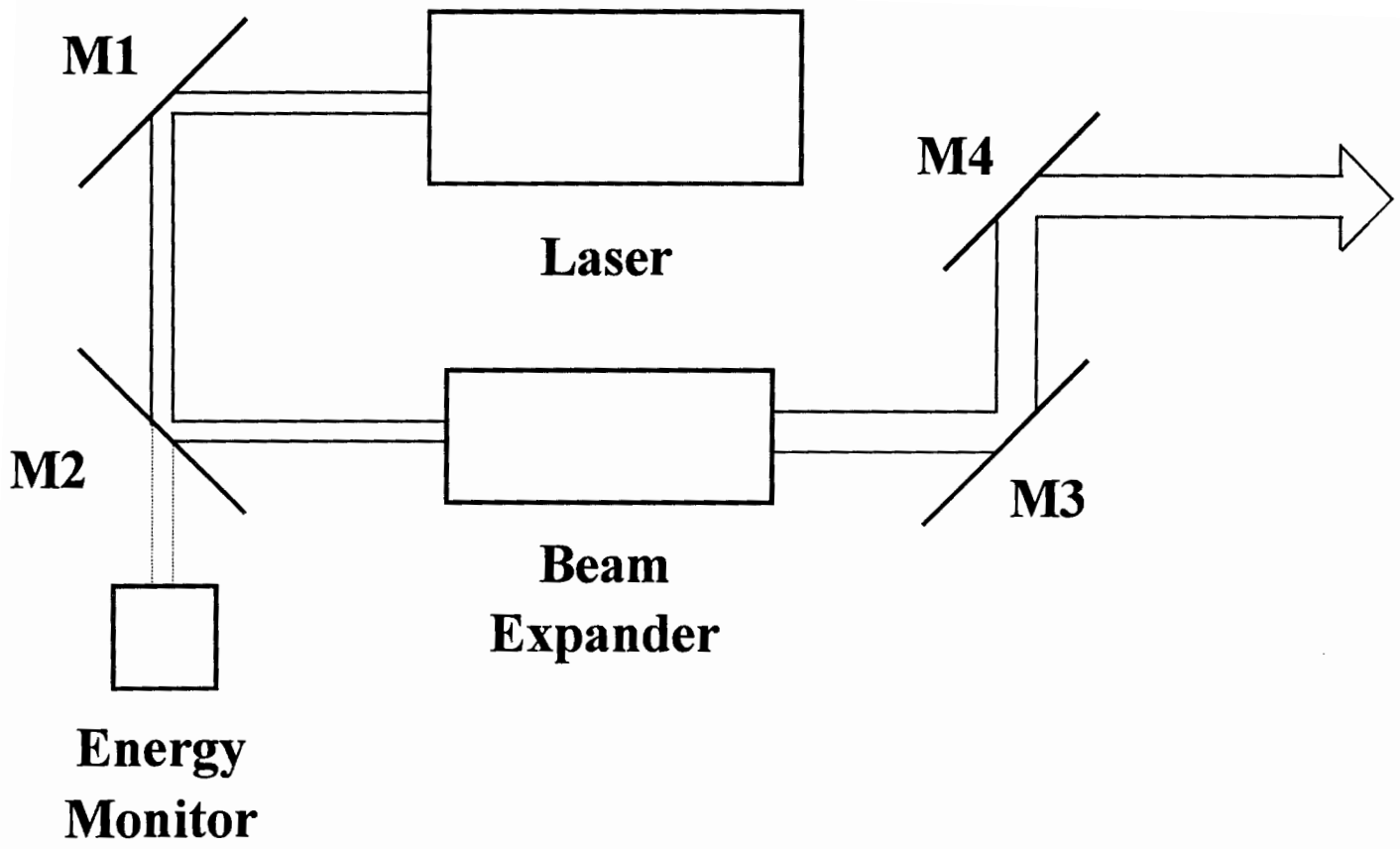

Figure 2.1. LARS Scanning Lidar Transmitter System

from 7 mm to 35 mm diameter. This reduces the energy density for safety purposes. It also reduces the divergence of the beam from 0.6 mrad to 0.12 mrad which keeps the beam from becoming too wide at higher altitudes (or longer range). Otherwise the received image of the beam would overflow the optical fibers and less energy would be coupled into the detector system.

After the beam expander, the beam is steered by two 4" diameter laser hard coated mirrors to align it with the axis of the telescope field of view and is transmitted into the atmosphere.

2.2 Optical Efficiency

The number of photons emitted at each wavelength is calculated by dividing the emitted energy E_L by the energy of a photon hc/λ_L . This value is included in the lidar equation (Eq. 1.2) as term (2). This term, by itself, neglects losses from the beam steering mirrors and the beam expander. These losses are accounted for by including an efficiency term, η_{trans}. The optical efficiencies of each of the optics is listed in Table 2.2. The 1064 nm and 355 nm beams are linearly polarized horizontally with respect to the optical table. The 532 nm beam is linearly polarized vertically with respect to the optical table. All of the beam steering mirrors were identically coated, and thus have the same reflection efficiency.

Table 2.2. Transmitter Optical Efficiencies

	@1064 nm	**@532 nm**	**@355 nm**
Mirror #1[1]	$R_{\parallel} = 0.96$	$R_{\perp} = 1.0$	$R_{\parallel} = 0.77$
Mirror #2[1]	$R_{\parallel} = 0.96$	$R_{\perp} = 1.0$	$R_{\parallel} = 0.77$
Beam Expander[2]	$T_{min} = 0.92$	$T_{min} = 0.92$	$T_{min} = 0.96$
Mirror #3[1]	$R_{\perp} = 0.99$	$R_{\parallel} = 0.93$	$R_{\perp} = 0.81$
Mirror #4[1]	$R_{\perp} = 0.99$	$R_{\parallel} = 0.93$	$R_{\perp} = 0.81$
Total Efficiency	$\eta_{1064} = 0.83$	$\eta_{532} = 0.79$	$\eta_{355} = 0.38$

[1] All Mirror reflectances measured on Hitachi spectrophotometer.
[2] Beam expander reflectance values taken from specifications.

2.3 Energy Monitor

In the lidar equation, the energy of the laser source is assumed to remain constant, however, lasers actually exhibit some degree of power fluctuations over time. Failure to consider these fluctuations can result in significant errors in the results. To monitor and compensate for these fluctuations, an energy monitor is placed behind the first beam steering mirror. A small percentage of the laser energy passes through the mirror instead of being reflected.

The energy monitor consists of three channels. Three photodetectors with narrowband filters to separate the three emitted wavelengths are placed behind a optical diffusing arrangement. The power of each wavelength is continuously monitored and stored with the raw data file so that the data acquisition and processing system can correctly account for power fluctuations.

Chapter 3

Receiver System Efficiency

3.1 The Receiver System

Photons from the transmitted laser beam interact with atmospheric particles and are either absorbed or re-emitted. Photons that are scattered back towards the receiver are collected by the receiver system and coupled into the detector system. A schematic drawing of the receiver system is shown in Figure 3.1

3.1.1 The Telescope

A 16" diameter, f/7.8 Ritchey-Chrétien telescope is used to collect the backscattered light. A Ritchey-Crétien telescope is a type of Cassegrain telescope that uses hyperboloid primary and secondary mirrors, which has the advantage of a compact design. The short length makes it suitable for use on the scanning optical table. The small secondary mirror allows the laser beam to become unobstructed quicker so results can be obtained at closer range. In general, Ritchey-Crétien telescopes are coma free but do suffer from astigmatism and curvature of field. Since the telescope is being used to just collect the scattered photons, the imaging quality of the telescope is not important, and the aberrations are of only minor concern.

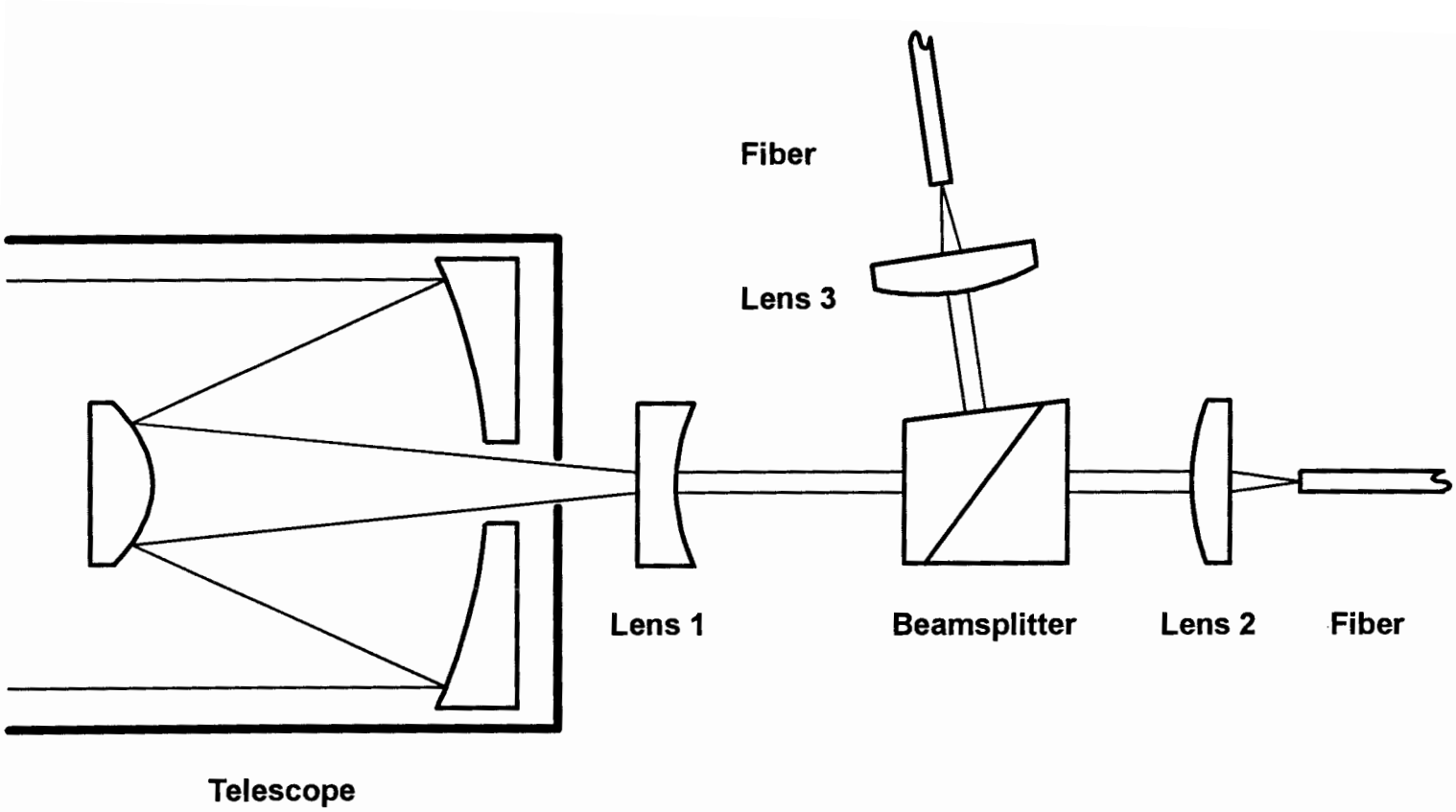

Figure 3.1. LARS Scanning Lidar Receiver System

3.1.2 Polarization Beamsplitter

A Glan-Air polarizing beamsplitter is used to separate the orthogonal polarization components because it is capapable of separating the polarization components independent of wavelength. The beamsplitter consists of two wedges of calcite separated by an air gap. The optical axes of the wedges are oriented parallel to the entrance surface. Because calcite is bifringent, the orthogonal polarization components experience different indices of refraction in the calcite. The angle of the calcite-air interface is chosen such that the extraodinary-ray (p-polarization) is passed, but the ordinary-ray (s-polarization) is totally internally reflected (see Chapter 4 for explanation of total internal reflection). The o-ray is reflected out of the crystal at 75.2°. The side output surface is also at 75.2° so that there is no angular separation of the different output wavelengths caused by dispersion.

The beamsplitter works best if the input light is collimated. A 60 mm focal length plano-concave lens is used to collimate the converging beam from the telescope. To keep the distance behind the telescope a minimum, the lens was chosen to produce a collimated beam with a diameter of 8 mm, the largest size beam that will be slightly smaller than the beamsplitter's clear aperture.

3.1.3 Fiber Coupling

Each polarization component is coupled into separate multi-mode fibers which are connected to the detector system. Plano-convex converging lenses with 32 mm focal length are used to focus the beams into the optical fibers. Alignment of the fiber coupling system is critical for good performance. This point will be further discussed in Chapter 4.

3.2 Optical Efficiency

The collecting area of the receiver telescope is the primary parameter determining the sensitivity of the receiver system. This is included in the lidar equation, Eq. 1.2, in term (5). A larger telescope would collect more light and improve the system performance. However, a larger telescope would be prohibitively heavy and would take too much space on the scanning table, not to mention the extra cost. Once the telescope size was selected, 16" diameter, the optical efficiency of the receiver system becomes the next critical performance factor.

The efficiency of the receiver can be evaluated in two parts. The wavelength and polarization dependent components can be evaluated based on the properties of the materials used for the optical components. The efficiency also has a range dependent component that can be evaluated by considering the telescope geometry and reception probability. As will be explained in Section 3.2.2, the range dependent efficiency has been included as a separate term in the lidar equation, $\xi(R)$.

3.2.1 Material Properties of Optical Components

The efficiencies of the receiver optics are shown in Table 3.1. The fused silica lens are almost completely transparent, but suffer from surface reflections. To improve the efficiency of the system these lenses could be AR (anti-reflection) coated.

Table 3.1. Receiver Optical Efficiencies

Optical Element	**@1064 nm**	**@607 nm**	**@532 nm**	**@355 nm**
Telescope[1] (x2 Al(SiO_2) mirrors)	0.92^2 = 0.85	0.88^2 = 0.77	0.89^2 = 0.79	0.90^2 = 0.81
Collimating Lens[2] (fused silica)	0.93	0.93	0.93	0.93
Beamsplitter[3]				
P-polarization (trans)	0.96	0.96	0.96	0.96
S-polarization (refl)	0.73	0.73	0.73	0.73
Focusing Lens[2] (fused silica)	0.93	0.93	0.93	0.93
Total Efficiency				
P-polarization	$\eta_{1064} = 0.71$	$\eta_{607} = 0.64$	$\eta_{532} = 0.67$	$\eta_{355} = 0.67$
S-polarization	$\eta_{1064} = 0.54$	$\eta_{607} = 0.49$	$\eta_{532} = 0.50$	$\eta_{355} = 0.51$

[1] from manufacturer's specifications.
[2] Calculated from Fresnel equations for normal reflection at a boundary surface
[3] measured with laser at 543nm

3.2.2. Telescope Geometry and Reception Probability

As stated in term (5) of the lidar equation, the photon collecting power of the telescope is a factor of the primary mirror area (A_0/R^2) and the reception probability ($\xi(R)$). The reception probability has many factors that make it range dependent. Divergence of the laser beam, obscuration by the secondary mirror, chromatic aberration of the collimating and focusing lenses, and the field stop of the fiber diameter all affect the probability that photons from a given range will be collected. The normalized form factor of the receiver probability is shown in Figure 3.2.

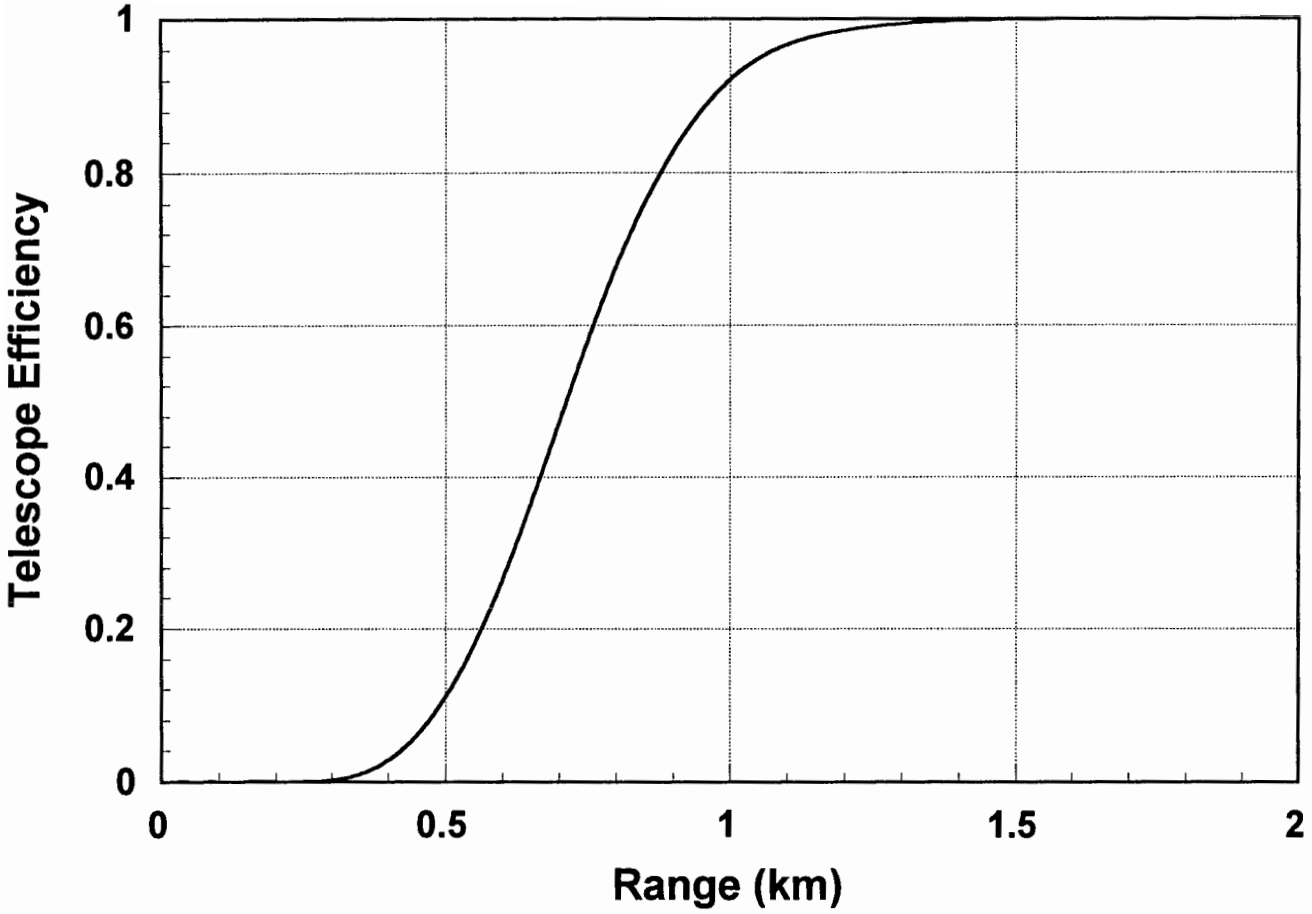

Figure 3.2. Efficiency of the LARS receiver telescope

Chapter 4

Receiver/Detector Fiber Coupling System Efficiency

The LARS system uses an optical fiber to couple the light from the receiver system to the detector system. In many laser remote sensing systems, the detector is placed directly in the optical path of the receiving system, or the light is steered by mirrors to the detector system. Using optical fiber offers many advantages over these other methods.

The most important advantage of using an optical fiber is that the detector system is remotely located inside the field laboratory instead of on the scanning platform. This greatly reduces the size and weight of the table. The detector system itself weighs over 150 pounds and consists of two 25" x 13" x 7" boxes with photodetectors attached to one side. If the detector system were to be placed behind the telescope, the scanning table would have to be larger. The extra weight of the detector boxes and table would necessitate a more complex and more expensive scanning system.

There are also fewer cables between the scanning platform and the field laboratory. Only the two optical fibers are connected from the receiver system on the scanning platform to the detector system in the laboratory. This is much better than the multiple coaxial cables that would have to be connected to the data acquisition system and power supplies if the detector system were on the scanning platform. Having the detector system in the field laboratory also protects it from the outside environment. Sharp temperature changes, vibrations from scanning and precipitation can all be damaging to the detector system.

Optical fibers have a significant effect on the efficiency of the lidar system. To understand these effects it is necessary to understand the principles of light propagation in a fiber.

4.1 Light Propagation in a Multimode Fiber

A multimode stepped-indexed optical fiber consists of a cylindrical core of dielectric surrounded by another dielectric layer, called the cladding, with a smaller index of refraction. Light that enters the fiber can be totally internally reflected at the boundary of the core as illustrated in Figure 4.1. The angle of refraction at the core-cladding interface can be determined according to Equation 4.1, Snell's Law.

$$\theta_1 = \frac{n_2}{n_1} \sin\theta_2 \qquad (4.1)$$

When $\theta_2 = 90°$, $\sin\theta_2 = 1$ and $\sin\theta_1 = n_2 / n_1$. This angle is know as the critical angle, θ_c. When θ_1 is greater than or equal to the critical angle, all of the incident light will be reflected. The optical fiber will act as waveguide, carrying the light to the detector system with little attenuation.

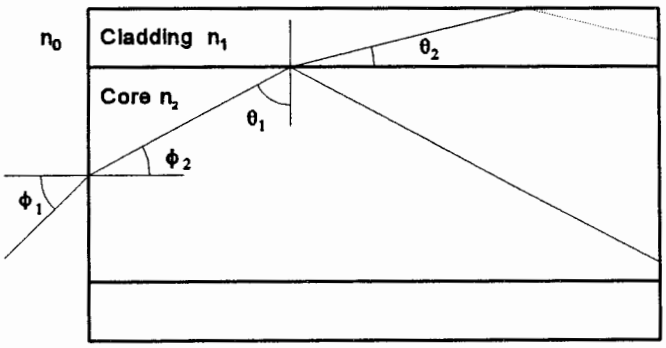

Figure 4.1. Total internal reflection inside an optical fiber

4.1.1 Acceptance Angle

Using Snell's law (Eq. 4.1) at the end of the fiber, the cone of accepted light that will be totally reflected can be derived. The maximum input angle at which light will be totally reflected (ϕ_{max}) is know as the acceptance angle. The acceptance angle is related to the numerical aperture (NA), a quantity that measures the light gathering power of the fiber. The numerical aperture is calculated from the index of refraction of the fiber materials in Equation 4.2.

$$NA = n_0 \sin\phi_{max} = (n_f^2 - n_c^2)^{1/2} \qquad (4.2)$$

Since the index of refraction of the core and cladding materials is wavelength dependent, the numerical aperture will also be wavelength dependent.

The calculated value for the numerical aperture is only valid for long fiber lengths (steady state). For short fibers the numerical aperture can be larger because some of the light from larger angles will be partially reflected at the core boundary and some will enter the cladding layer and be guided. For short distances these light rays will not be completely attenuated.

The acceptance angle for the LARS fiber coupler needs to be considered in two ways. At the receiving telescope end, the focusing lens should be selected so that all of the light received can be coupled into the fiber. If the lens is too fast, some of the rays will enter the fiber at an angle greater than the acceptance angle and will not be guided. At the detector end, the light will exit the fiber in a cone that is identical to the acceptance cone. The f/# (focal length/diameter) of the collimating lens should be chosen so that all of the light is

collimated by the lens. In both cases, it is necessary to match the numerical apertures of the lenses with the numerical aperture of the fiber. The numerical aperture of a lens is related to the f-number by $f/\# = (2NA)^{-1}$.

4.1.2 Propagation Delay and Modal Dispersion

Since range information is derived from the time it takes for the photons to travel out into the atmosphere and back to the detector system, failure to consider propagation time through the fiber would produce a significant error in the range values. Propagation time is dependent upon the path taken through the fiber. The different paths light can take through the fiber are called guided modes or propagation modes. Light traveling straight through the fiber would take less time to arrive at the output end than light that enters at an angle, whose speed would be reduced by $\cos(\theta)$. Also, each wavelength of light will take different times to propagate through the fiber because the index of refraction is wavelength dependent. The differences in arrival time caused by these delays are called intermodal dispersion and chromatic dispersion, respectively.

The average propagation delay can be calculated by multiplying the fiber length by the index of refraction of the fiber core. The maximum dispersion (Δt_{max}) can also be calculated. Dispersion will cause a loss of range resolution since photons returning from one altitude will return in a broadened time interval. Propagation delay and dispersion for the LARS system will be discussed in Section 4.2.

4.1.3 Mode Coupling

In an ideal fiber, the orthogonal polarization components would be preserved; however variations in refractive index, imperfections in the circular geometry, and bends or twists will cause coupling between the polarized modes in a real fiber (Allard 1990, p1.46). For the LARS system this is a desirable effect. Once the polarization components are separated, we are only interested in the intensity of the signals. Since the polarization is mixed in each fiber, the output of each fiber differs in intensity only. Otherwise the detector system's efficiency would be different for each of the detector boxes and would be more difficult to determine. Since the detector boxes are identical, the detector efficiencies should also be the same.

The guided modes will also be coupled in a real optical fiber. Some photons will be guided into radiative modes and will be absorbed by the fiber, but most will be coupled into other guided modes. Thus, the exit angle for a given ray will not necessarily be the same as its entry angle. Assuming that the fiber thoroughly mixes the modes, the output pattern will be uniform through the cone with maximum angle θ_c (the critical angle).

The loss of output intensity due to coupling into radiative modes can be caused by micro-bending. It is important that the optical fiber not be bent at great angles or that no kinks develop. A surrounding steel cable should reduce the amount of bending losses.

4.2 Optical Efficiency

The optical fiber used with LARS has a fused silica core with a plastic cladding layer and a nylon jacket surrounding the cladding for protection. An additional stainless steel mesh

cable surrounds the fiber for extra protection, since the cable will be connected between the scanning platform and the field laboratory. The nominal specifications for the optical fiber used in LARS are shown in Table 4.1.

Table 4.1: Superguide PCS UV-Vis Fiber (Fiberguide Industries)

Fiber Layers Core diameter (fused silica) Cladding diameter (plastic)	 1000 um 1150 um			
Length	10 meters			
	@1064 nm	**@607 nm**	**@532 nm**	**@355 nm**
Index of Refraction (n_{core})[1]	1.4496	1.4578	1.4607	1.4761
Numerical Aperture (NA)[2]	0.388	0.391	0.389	0.382
Transmission[1] (for 10 m of fiber)	0.95	0.97	0.96	0.67
Surface Reflectance[3]	0.034	0.035	0.035	0.037
Total Efficiency	0.89	0.90	0.90	0.62

[1] Derived from manufacturer's specifications
[2] From manufacturer's measurements for a short fiber (5-10 meters)
[3] Calculated from Fresnel equations for normal reflection at a boundary surface

The values for transmission through the fiber only consider attenuation from absorption and scattering in the fused silica core. External transmittance would include losses from surface reflections at both fiber ends (under 4% per surface). Thus, the total optical efficiency at each wavelength considers both internal losses and surface reflection losses. There can also be a significant decrease in efficiency from fiber misalignment (see Section 4.2.3).

4.2.1. Propagation Delay and Dispersion

Theoretically, the shortest delay through the fiber would occur for a 1064 nm photon traveling straight through the fiber because it experiences the smallest index of refraction in fused silica and takes the shortest path through the fiber. The longest delay would be for a 355 nm photon entering at the critical angle because it experiences the largest index of refraction in fused silica and takes the longest path through the fiber.. The propagation delays are calculated from the relation,

$$\tau = \frac{nl}{c \cdot \cos\theta} \qquad \textbf{(4.3)}$$

where n is the index of refraction, l is the length of the fiber, c is the speed of light, and θ is the entry angle. Therefore, the minimum and maximum transit times through the optical fiber are,

$\tau_{min} =$ 48.3 ns ,

$\tau_{max} =$ 53.3 ns ,

Maximum dispersion $\equiv \Delta\tau_{max} = \tau_{max} - \tau_{min} =$ 5 ns ,

Average propagation time = $(\tau_{max} + \tau_{min})/2 =$ 50.8 ns .

Range information is calculated from the time it takes for a photon to travel from the transmitter to a scattering element and back to the detector system. Since the data is integrated by the data acquisition system in 100 ns bins, the range resolution is 15 m. The average propagation time accounts for a +7.6 m bias in the range. Dispersion causes a

smearing over 0.75 m, which is negligible compared to the 15 m averaging of the data acquisition system.

4.2.2 Fiber Alignment

The alignment between the receiver focusing lenses and the optical fibers is critical to obtaining high efficiency. The optical fiber is mounted to an xyz translation stage so that it can be correctly aligned. If the center of the optical fiber is not aligned with the optical axis of the focusing lens, some of the focal spot will image outside the fiber core and the light will be lost. Figure 4.2 shows an example of alignment efficiency for different fiber positions. As the fiber becomes more misaligned, the efficiency decreases rapidly. Measurements were taken with the Penn State Applied Research Lab's LAMP lidar system. Fiber misalignments are also dependent upon the range. The far field spot size is much smaller than the near field spot size. Small misalignments will be noticed in the near field but not in the far field.

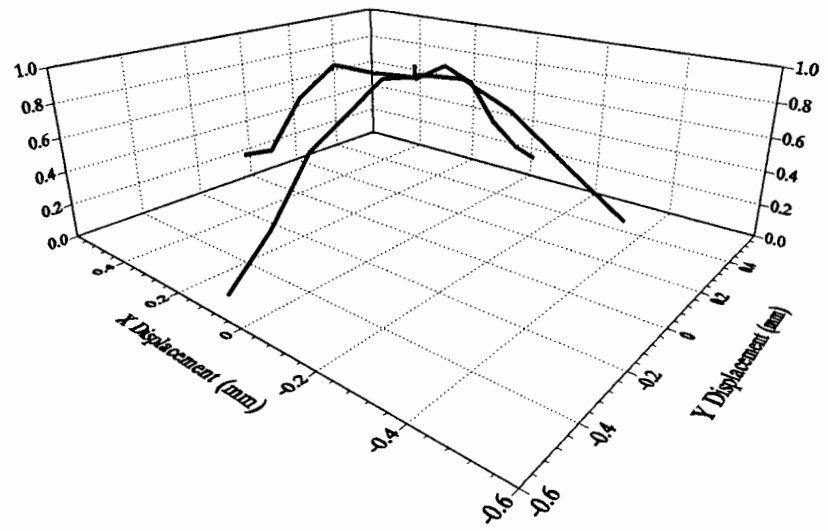

Figure 4.2. Normalized Efficiency vs. Displacement of Fiber from Optical Axis

To keep the fibers aligned with the focus of the coupling lenses, an automatic positioner has been designed. This automatic positioning system uses a quadrant photodetector with the fiber inserted into the center. When the fiber is not aligned correctly, more light will illuminate one quadrant of the photodetecter than the others. The positioning system will drive motorized micropositioners to adjust the fiber's position until the light distribution upon the quadrant photodetector is uniform.

Chapter 5

Detector System Efficiency

5.1 The Detector System

The detector system has two primary functions. First, the detector system must separate the spatially overlapped signals from each other and the background light. Then the light signals must be converted into electrical signals so that they can be processed by the data acquisition and processing system. Defining the detector system as such, the polarization cube from the receiver system is actually part of the detector system since it separates the polarization components of the return signal. For simplicity, however, it is as easy to consider the polarization beamsplitter as part of the receiver system. Since the fiber coupler mixes the polarization of the light signals as they pass through, the detector systems behave similarly for each of the polarization components. Actually, the detector boxes for each polarization were designed to be identical except for one minor detail; the 607 nm Raman channels is used in only one box. A schematic diagram of the detector system is illustrated in Figure 5.1. A key to the components in the detector system follows the figure.

5.1.1 Separating the Optical Signals

The return light from the atmosphere will consist of several wavelengths of interest, 1064 nm, 607 nm, 532 nm, and 355 nm. There will also be background noise from lights, the sun, etc. Each of these signals is separated in the detector box to illuminate different photodetectors.

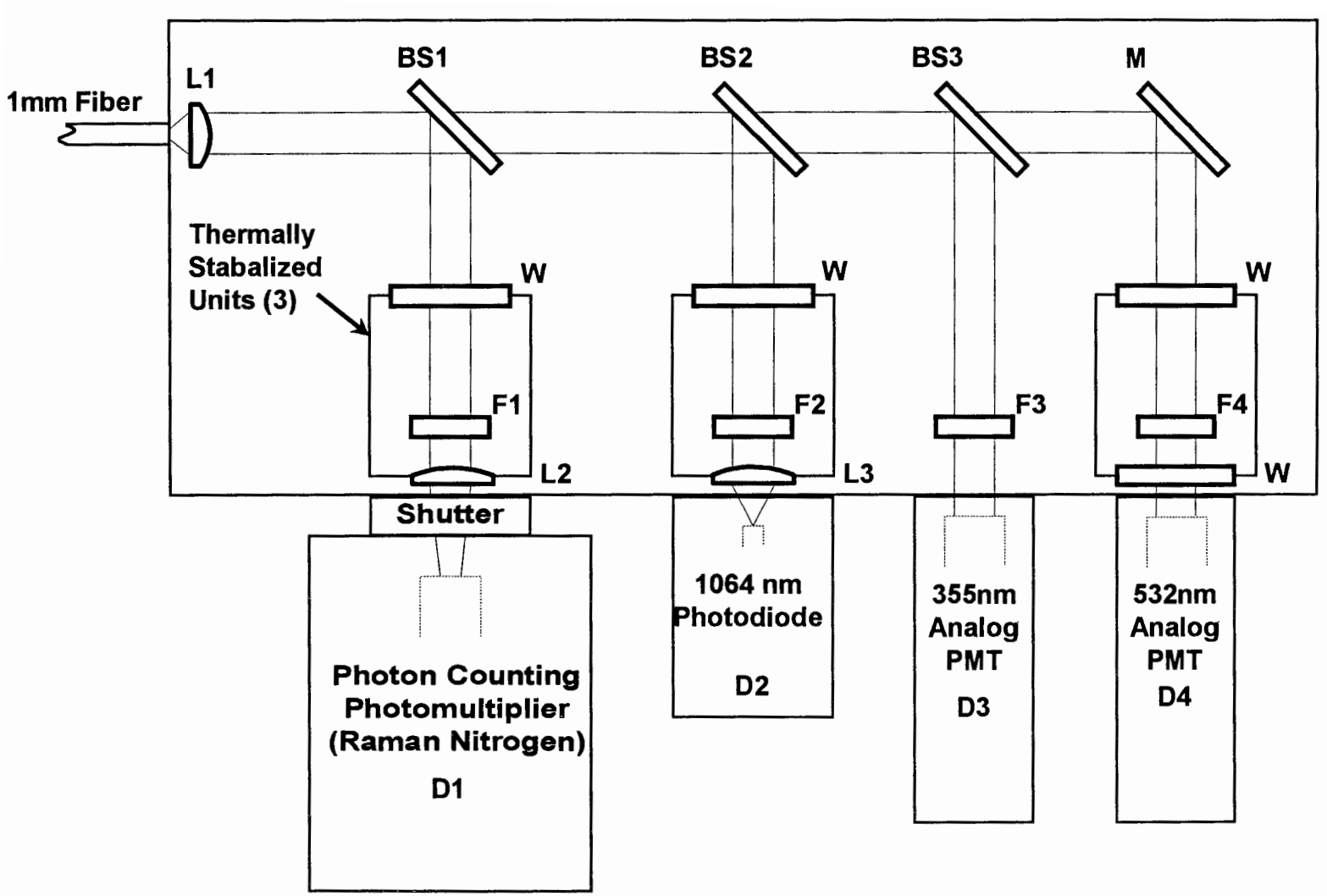

Figure 5.1. LARS Scanning Lidar Detector Box

Key to Figure 5.1

L1 plano-convex lens, d = 25 mm, f = 33 mm (@589 nm), UV grade fused silica

L2 plano-convex lens, d = 25 mm, f = 88.3 mm, BK7

L3 plano-convex lens, d = 25 mm, f = 50.2 mm, BK7

BS1 dichroic beamsplitter, d = 50 mm, reflect @ 607 nm, transmit @ 355, 532, 1064 nm

BS2 dichroic beamsplitter, d = 50 mm, reflect @ 1064 nm, transmit @ 355, 532 nm

BS3 dichroic beamsplitter, d = 50 mm, reflect @ 355 nm, transmit @ 532 nm

M flat mirror, d = 50 mm, Al(MgF_2) coated broadband

W window, d = 25 mm, BK7

F1 narrowband filter, d = 25 mm, 607.3 nm peak @35°C, 0.35 nm bandwidth, flouride 3 cavity, 0.025nm/°C thermal coefficient

F2 narrowband filter, d = 25 mm, 1064.0 nm peak @23°C, 1.0 nm bandwidth, 2 cavity, 0.025nm/°C thermal coefficient

F3 narrowband filter, d = 25 mm, 354.7 nm peak @23°C, 1.0 nm bandwidth, oxide 3 cavity, 0.0025nm/°C thermal coefficient

F4 narrowband filter, d = 25 mm, 532.0 nm peak @35°C, 0.35 nm bandwidth, fluoride 3 cavity, 0.025nm/°C thermal coefficient

D1 photon counting photomultiplier tube, cooled to -20°C, 9mm effective area S20 photocathode, 14 stage (dynodes)

D2 Si PIN photodiode, 5 mm dia. active area, QE = 50% @ 1064 nm

D3 analog photomultiplier tube, 23 mm biakali photocathode, 11 stage

D4 analog photomultiplier tube, 23 mm biakali photocathode, 11 stage

Collimation

The light output from the multimode fiber fills a cone with the maximum angle being the acceptance angle. The beam is collimated for maximum efficiency. This is especially important for eliminating noise when passing through the narrowband filters, which will be discussed further in Section 5.2.2.

To collimate the beam a short focal length lens is placed one focal length away from the end of the fiber. The beam is mostly, but not completely collimated by this lens. It would be difficult to completely collimate the beam for two reasons.

The first is that the fiber can not be considered a point object on the optical axis because it has a 1 mm diameter. For the fiber to approximate a point object, the lens would have to have a very long focal length. This would make the collimated beam diameter prohibitively large. The larger lenses, beamsplitters, and narrowband filters would be very costly. Also, the extra lengths in the detector box for the focal distance of the collimation lens and the lenses that would be needed to focus the collimated beams on the photodetectors would make the detector box prohibitively large.

The second reason the beam is not completely collimated is the chromatic aberration of the collimating lens. Each of the signals has a different focal length because of the wavelength dependence of the index of refraction. Table 5.1 shows the refractive index and focal length of the collimating lens for each of the signal wavelengths. Since the wavelengths are to be separated, it is not critical to collimate all of the wavelengths with the first collimating lens. This is fortunate because it would be difficult to find an achromatic lens that would meet the necessary specifications. Instead, the first lens need only collimate the first

channel that is separated, which would be the 607 nm wavelength. Even though it is only used in one of the detector boxes, collimating both boxes for 607 nm offers the advantage of identical arrangements and efficiencies. After the first beamsplitter, when the 607 nm signal has been removed from the combined signal, another lens can be placed to collimate the 1064 nm channel, which is next to be separated. Lens can be placed after the next two beamsplitters to do the same for the 355 nm and 532 nm signals.

Table 5.1. Index of Refraction for Collimating Lens

Wavelength	**Index of Refraction**	**Focal Length**
1064 nm	1.4496	33.65 mm
607 nm	1.4578	33.04 mm
532 nm	1.4607	32.84 mm
355 nm	1.4761	31.77 mm

Wavelength Separation

Dichroic beamsplitters are used to separate each of the optical signals. Dichroic beamsplitters function similar to narrowband thin film filters, which are discussed in the next section (noise filtering). Thin dielectric layers are stacked on a substrate in a manner that leads to high reflection of some wavelengths, and high transmission of others. Ideally the beamsplitters would totally reflect only the desired wavelength and transmit all other wavelengths. Real dichroic beamsplitters have complex reflection spectra. Spectral curves for each of the LARS dichroic beamsplitters can be found in the Appendix.

The beamsplitters are placed at a 45° angle with respect to the collimated signal beam,

so that light at the desired wavelength is reflected at 90°. Precise mounting equipment is used because the transmission spectrum is highly dependent upon the incident angle for the beamsplitters (and the narrowband filters).

Noise Filtering

Narrow band interference filters are used to remove all unwanted light from each of the optical signals by only transmitting a single wavelength (actually, a narrow band of wavelengths centered at the desired wavelength). Interference filters are created by stacking thin film layers on a glass substrate. When two highly reflective layers are separated by a dielectric or metal layer, they act like a Fabry-Perot interferometer. The thickness and refractive index of the filling layer determines the filter's transmission band. Fabry-Perot cavities have a Lorentzian shaped transmission curve. To increase the out-of-band blocking and to decrease the bandwidth, multiple Fabry-Perot cavities are stacked on the substrate. This improves blocking but decreases the peak transmission of the filter.

5.1.2 Converting to Electrical Signal

Once the optical signals are separated they must be converted to electric signals to be processed by the computer. Two different types of detectors are used in LARS, photomultiplier tubes and photodiodes.

Photomultiplier tubes (PMT's)

Photomultiplier tubes are used for most of the signal channels because they have a large active area and high gain. When a photon strikes the sensing surface, called the photocathode, an electron is emitted due to the photoelectric effect. The electron is accelerated by a strong electric field between the photocathode and an electrode called a dynode. When the electron impacts the dynode, several secondary electrons are ejected. The electrons are then accelerated toward another dynode and the process repeats. A typical PMT can have 6-14 dynodes. After impacting each of the dynodes, the electrons are collected by an anode. The output current amplification is the product of the individual dynode gains, and typically ranges between 10^6 and 10^8.

Very sensitive, high speed PMT's that are able to sense individual photons are called photon counters. A photon counting PMT is used for the nitrogen (607 nm) channel because of the low intensity of the return signal. In the other channels, the return signal is too large to resolve individual photons, so analog (current signal) PMT's are used.

Silicon Photodiodes

The performance of photomultipliers decreases significantly in the near infrared as the sensitivity of the photocathode rapidly decreases. For the 1064 nm Rayleigh scattering channel a silicon PIN photodiode is used instead. When a photon with energy greater than the band gap energy strikes in the depletion layer of a p-n junction, an electron-hole pair is created. The electric field in the junction causes the carriers to accelerate out of the junction. This produces a current which is proportional to the amount of incident light. In a PIN

photodiode, an intrinsic layer (i layer) with high resistance is added between the p and n layers. This improves the response time of the photodiode.

Another type of photodiode, the avalanche photodiode (APD), can be used instead. In the depletion layer of an APD, the electric field is strong enough to cause the accelerated electrons to collide with lattice atoms and release secondary electrons which repeat the process by freeing more electrons. This continues until the electron drifts out of the depletion layer and recombines with a hole. The avalanche effect provides an internal amplification of the optical signal.

Currently, PIN photodiodes are being used in LARS because there are infrared-enhanced PIN photodiodes commercially available. However, as discussed in Section 5.3.2, avalanche photodiodes may be a better choice because there is less noise in internal amplification than using an external operational amplifier.

5.2 Optical Efficiency

The maximum efficiency of the detector system can be determined by multiplying the efficiencies of each optical component separately. These results are shown in Section 5.2.1. Deviations from the maximum efficiency can occur for many reasons including poor alignment, thermal instability, and insufficient noise blocking. Some of the more critical deviations that can cause poor sensitivity or inaccuracies are considered in Section 5.2.2.

5.2.1 Path Efficiencies

As mentioned earlier, spectral curves for each of the detector optics are illustrated in the Appendix. The combined path transmission spectra for each of the channels is illustrated in Figure 5.2. The full ultraviolet-visible spectrum is shown to illustrate the out-of-band blocking of each channel. Blocking of the other channel wavelengths is very important to avoid bleed-through of the other signals. The near-infrared spectrum is not shown because of the measurement instrument's low SNR in the infrared. However, efficiencies at 1064 nm were still measured.

The resultant efficiencies for each wavelength are listed in Table 5.2. Since each optical channel consists of five to eight optical components, it is not surprising that the efficiencies are low (9%-25%). The narrowband filters affected efficiency the most. There is an unavoidable trade-off between a narrow transmission band and a high transmittance at the peak wavelength. In almost all of the channels, the combined out-of-band blocking was greater than the sensitivity of the spectrophotometer measurement instrument (10^{-5}).

Table 5.2. Detector System Channel Efficiencies

	355 Channel	**532 Channel**	**607 Channel**	**1064 Channel**
355 nm	**0.11**	$<10^{-5}$	$<10^{-5}$	$<10^{-5}$
532 nm	$<10^{-5}$	**0.14**	10^{-4}	$<10^{-5}$
607 nm	$<10^{-5}$	$<10^{-5}$	**0.25**	$<10^{-5}$
1064 nm	$<10^{-5}$	$<10^{-5}$	$<10^{-5}$	**0.087**

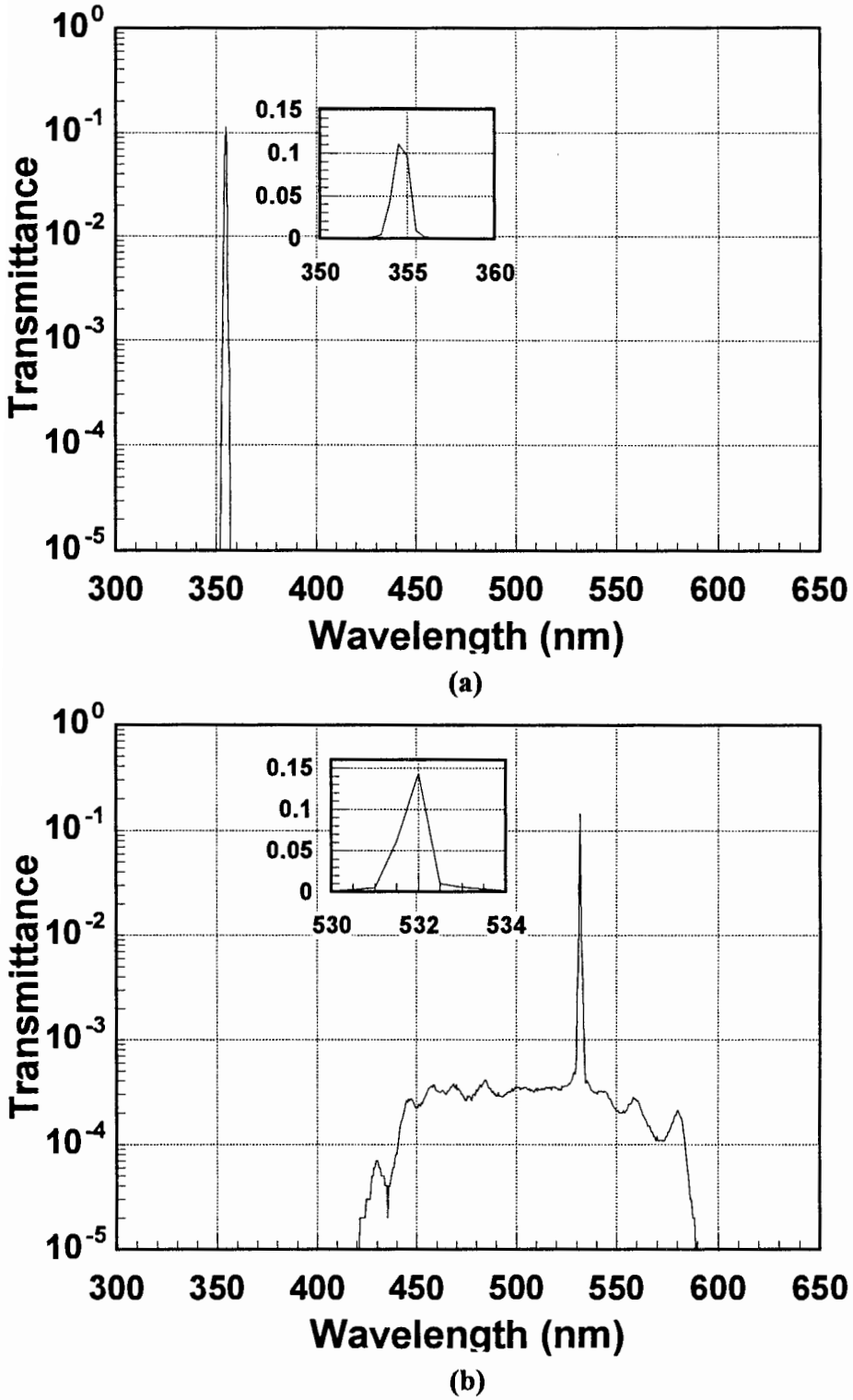

Figure 5.2. Total channel transmittance for (a) 355 nm (b) 532 nm (c) 607 nm and (d) 1064 nm

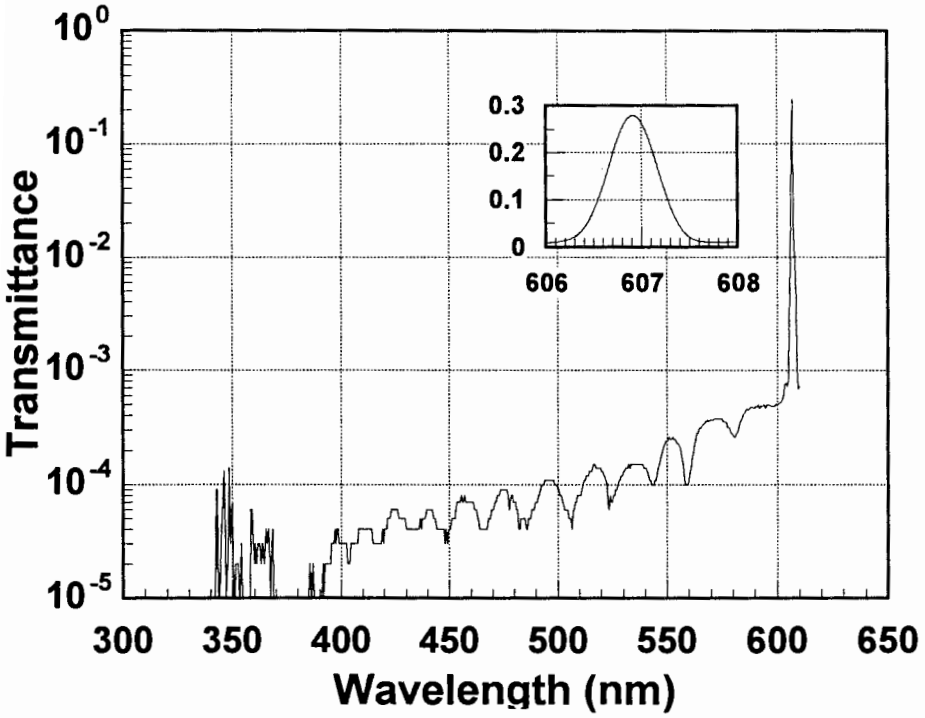
Transmittance
Wavelength (nm)
10^0
10^-1
10^-2
10^-3
10^-4
10^-5
300 350 400 450 500 550 600 650
0.3
0.2
0.1
0
606 607 608

(c)

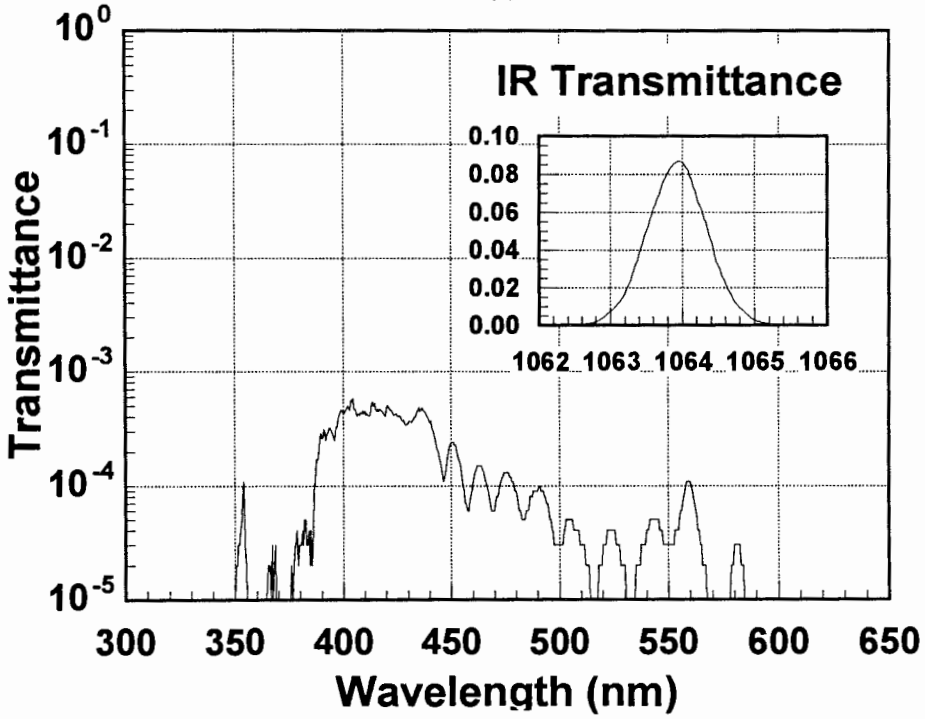
IR Transmittance
Transmittance
Wavelength (nm)
10^0
10^-1
10^-2
10^-3
10^-4
10^-5
300 350 400 450 500 550 600 650
0.10
0.08
0.06
0.04
0.02
0.00
1062 1063 1064 1065 1066

(d)

5.2.2. Variations in Optical Efficiency

The dichroic beamsplitters and narrowband filters are primarily responsible for the wavelength separation, and consequently, the optical efficiency of the detector system. Since they utilize interference effects from highly reflective surfaces separated by a precise distance, variations in this distance, or thickness in the case of thin film coatings, causes a significant wavelength shift in the spectral properties. The apparent thickness is affected by two parameters, the temperature of the optical component, and the incident angle of the illuminating light.

Wavelength Shifting with Temperature

An increase in temperature causes thermal expansion in the dielectric spacing material of the interference cavity. In the narrowband interference filters the transmittance peak wavelength will linearly increase with an increase in temperature. Figure 5.3 shows an example using the 607 nm narrowband filter. To keep the filter spectra stabilized, the filters are kept at a constant temperature, by putting them in heated mounts with a thermocouple controlled power supply. The filters are kept above the highest expected ambient temperature (currently 35°C) so that they will never be susceptible to temperature changes in any environment.

The amount of shifting can be calculated from the thermal expansion coefficient ($\Delta\lambda$/°C). The thermal expansion coefficient is dependent upon the initial peak wavelength of the filter. A typical curve of expansion coefficients is shown in Figure 5.4. The actual coefficients for each filter depend upon the materials and process used to fabricate the filter.

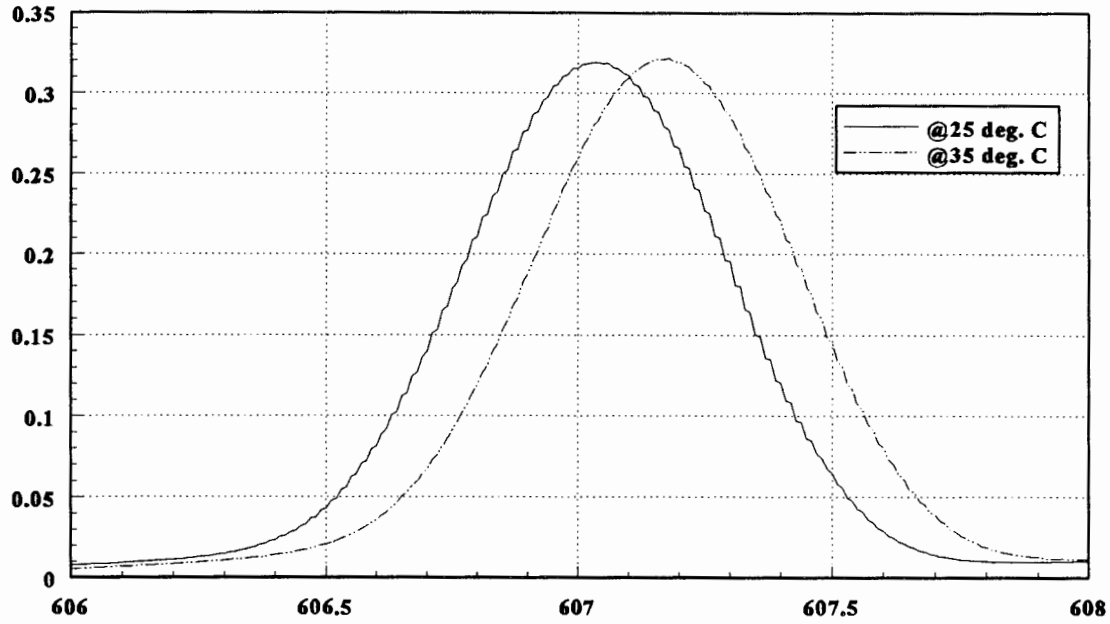

Figure 5.3. Wavelength shift of transmission spectrum with temperature

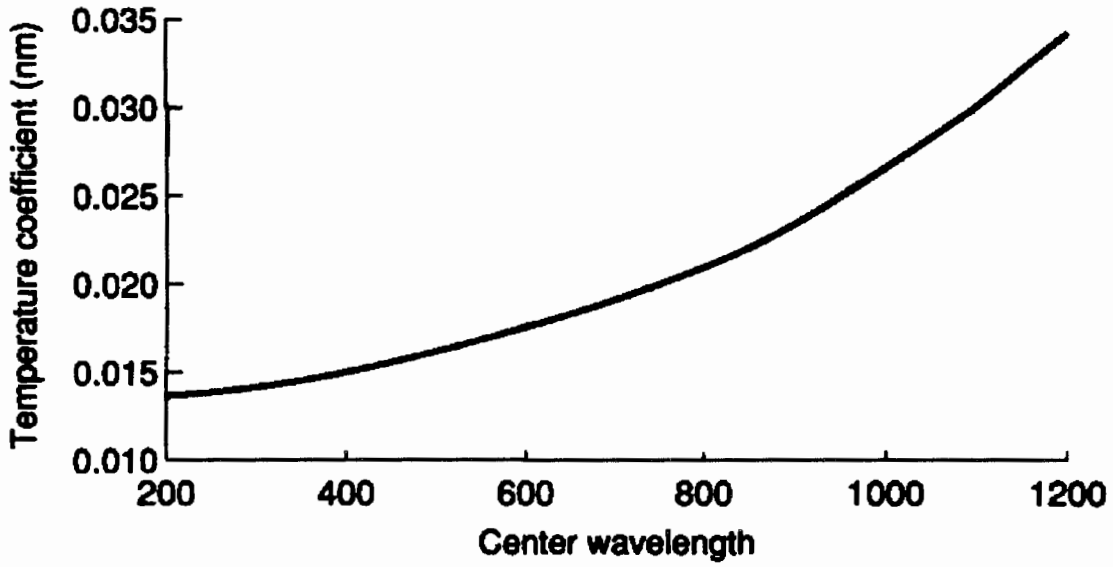

Figure 5.4. Typical thermal coefficient curve for narrowband interference filters (Andover Corp. 1992, p. 3)

Values are given in the key to Figure 5.1. Since the coefficient is small for the ultra-violet filter, the filter does not need to be thermally-stabilized.

Wavelength Shifting with Angle of Incidence

When light enters an interference filter at other than normal incidence, the center wavelength is shifted down. The change in center wavelength can be calculated with Equation 5.1 (Andover Corp 1992, p. 3).

$$\lambda_\theta = \lambda_0 \left[1 - \frac{\sin^2 \theta}{n_e^2} \right]^{\frac{1}{2}} \qquad (5.1)$$

θ = angle of incidence

n_e = effective refractive index of filter

This shifting with angle is why it is important to keep the light as close to collimated as possible in the detector system. Deviations from true collimation make the bandwidth of the filter wider and may decrease the transmission at the peak wavelength.

The beamsplitters need to be placed at exactly 45° with respect to the input beam for two reasons. Deviations from this angle will change the spectrum of the beamsplitter. Figure 5.5. illustrates an example of wavelength shifting with angle of incidence for an ultraviolet beamsplitter from the LAMP system. However, because the beamsplitters have wide transmission/reflection bands, small angular deviations may not cause much of a change at the signal wavelength. A more important reason to have the beamsplitters at 45° is to direct the

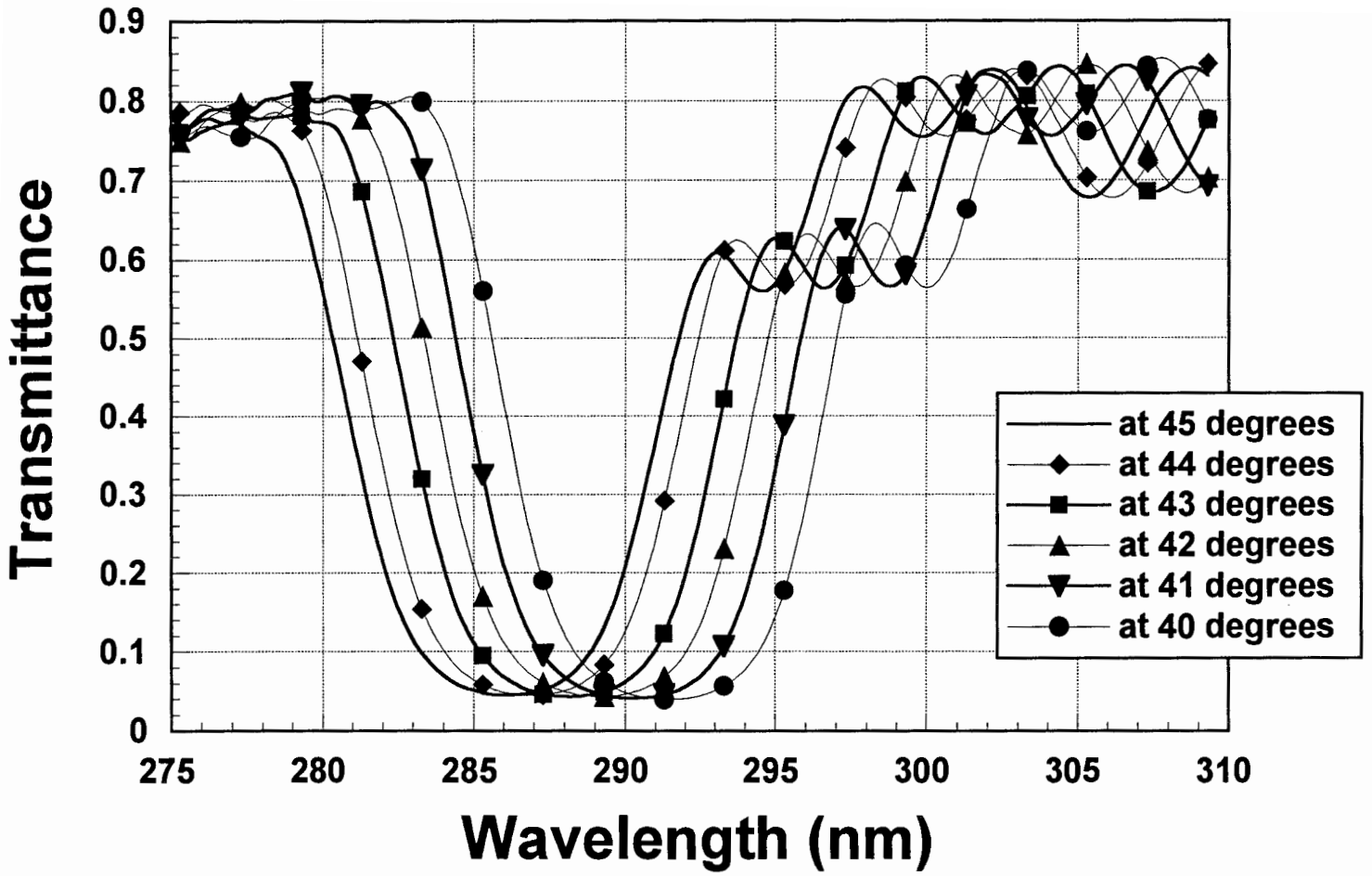

Figure 5.5. Wavelength shifting with angle of incidence for a 285 nm beamsplitter (Contributed by Steve McKinley)

optical signals to enter the narrowband filters at normal incidence. The angle shift could be useful for controlling the splitting edge for near components.

5.3 Detector Sensitivity

Photomultipliers and photodiodes have properties that limit their sensitivity to light. These properties ultimately limit the detecting abilities of a laser remote sensing system. Some of the critical detector specifications are listed in Table 5.3.

Table 5.3. Detector Specifications

Channel	**355 nm Channel**	**532 nm Channel**	**607 nm Channel**	**1064 nm Channel**
Device	Analog PMT	Analog PMT	Photon Counting PMT	PIN Photodiode
Quantum Efficiency (QE%)	27	14	7	50
Radiant Sensitivity (ma/W)	77	60	35	430
Max. Dark Current (nA)	2	2	300[1]	30
Response Time (ns)	15	15	2.5	26
Transit Time (ns)	80	80	45	n.a.

[1] counts per second

5.3.1 Quantum Efficiency and Radiant Sensitivity

The main factor of detector sensitivity is the quantum efficiency (QE%). The quantum efficiency is the average number of electrons emitted for each incident photon. This can also

be expressed as radiant sensitivity or responsivity, which is the current produced per watt of incident radiation. Responsivity is related to quantum efficiency by

$$Radiant\ Sensitivity = \frac{\lambda(nm)\, QE\%(\lambda)}{1.24}\ mA/W \quad . \tag{5.2}$$

5.3.2 Detector Noise

The detector system itself affects the output electric signal by adding noise to the signal. It is important to understand how this affects the minimum detectable power when selecting the photodetectors.

Thermal noise and shot noise

A thorough description of noise mechanisms in a laser remote sensing system is given by Measures (1992, pp. 223-236). For both PMT's and photodiodes, the total device noise is a combination of thermal noise (Johnson noise) and shot noise. Thermal noise is generated in the output resistor of the detector by the random thermal motions of the electrons. Shot noise (called generation-recombination noise in photodiodes) is caused by random fluctuations in the occurrence of photon (or electron) interactions in the photocathode, dynode, or depletion layer. Shot noise has two components, from the optical signal and from the dark current, which is the random thermal generation of current (photon counts) without an optical signal.

Typically for a weak signal, in a photomultiplier, the shot noise from the dark current

is greater than the thermal noise and signal shot noise and can be considered the primary noise limitation (after background noise, which will be discussed later). It is important to keep the dark current small, especially when photon counting. For the Raman 607 nm channel, the photon counting photomultiplier is cooled to -20°C to lower number of dark counts.

In the photodiode, thermal noise will be more significant. Because the photodiode has a low internal gain, an additional amplifier must be used. The thermal noise of the additional operational amplifier also contributes to the thermal noise of the detection channel.

To avoid the need of an external amplifier, the PIN photodiode could be replaced with an avalanche photodiode. In avalanche photodiodes, the internal gain mechanism multiplies the signal before the output resistor. If the gain is large enough, the shot noise will become the dominating noise mechanism.

Range Bias from PMT Transit Times

There is a time delay between when a photon strikes the cathode of a PMT and when the electrons generate a signal in the anode. Like the fiber propagation time (Sect. 4.2.1), the transit time must be considered when determining range information. Transit time accounts for a 15.2 m and a 8.6 m range bias in the analog and photon counting channels respectively.

Pulse Overlap in Photon Counting Detection

When more than one photon arrives at the photon counting detector at, or near, the same time, the resultant signal pulses can not be resolved and only appear as one photon count. This is known as pulse overlapping. Pulse overlap can occur in the photomultiplier,

the discriminator, or the data acquisition unit. The smaller the time constant of the component, the better it will be able to resolve pulses, hence, there will be less pulse overlap.

In general, photon counting should only be used when the optical signal is weak enough that individual photon pulses can be discriminated. Because of the random nature of photon arrival times, pulse overlap will still occur even in weak signals, but it will be less significant. Low photon count values can be corrected by determining the frequency of overlap by Poisson statistics.

Background Noise

Along with the return signal, there is also a background light component that enters the lidar receiver system. During the day, background light from the sky is the largest noise factor, far surpassing thermal noise or shot noise. Figure 5.6 shows solar irradiance at sea level as calculated from Lowtran 7. Lowtran 7 is a computer model, originated by the Air Force Geophysics Laboratory, for estimating transmittance, background radiance, and solar and lunar radiance with moderate resolution (20 cm^{-1}). Lowtran gives an averaged idea of expected day-sky background, but the actual background is extremely variable. Time of day, day of the year, solar angle, location, visibility, and solar activity are a few of the factors that affect the day-sky background

Several things can be done to keep background noise at a minimum. Using filters with very narrow bandwidths in the detector system eliminates noise from light at wavelengths other than the signal wavelengths. Limiting the field of view of the telescope to match the divergence of the transmitted beam reduces the receiver area for the noise, while not affecting

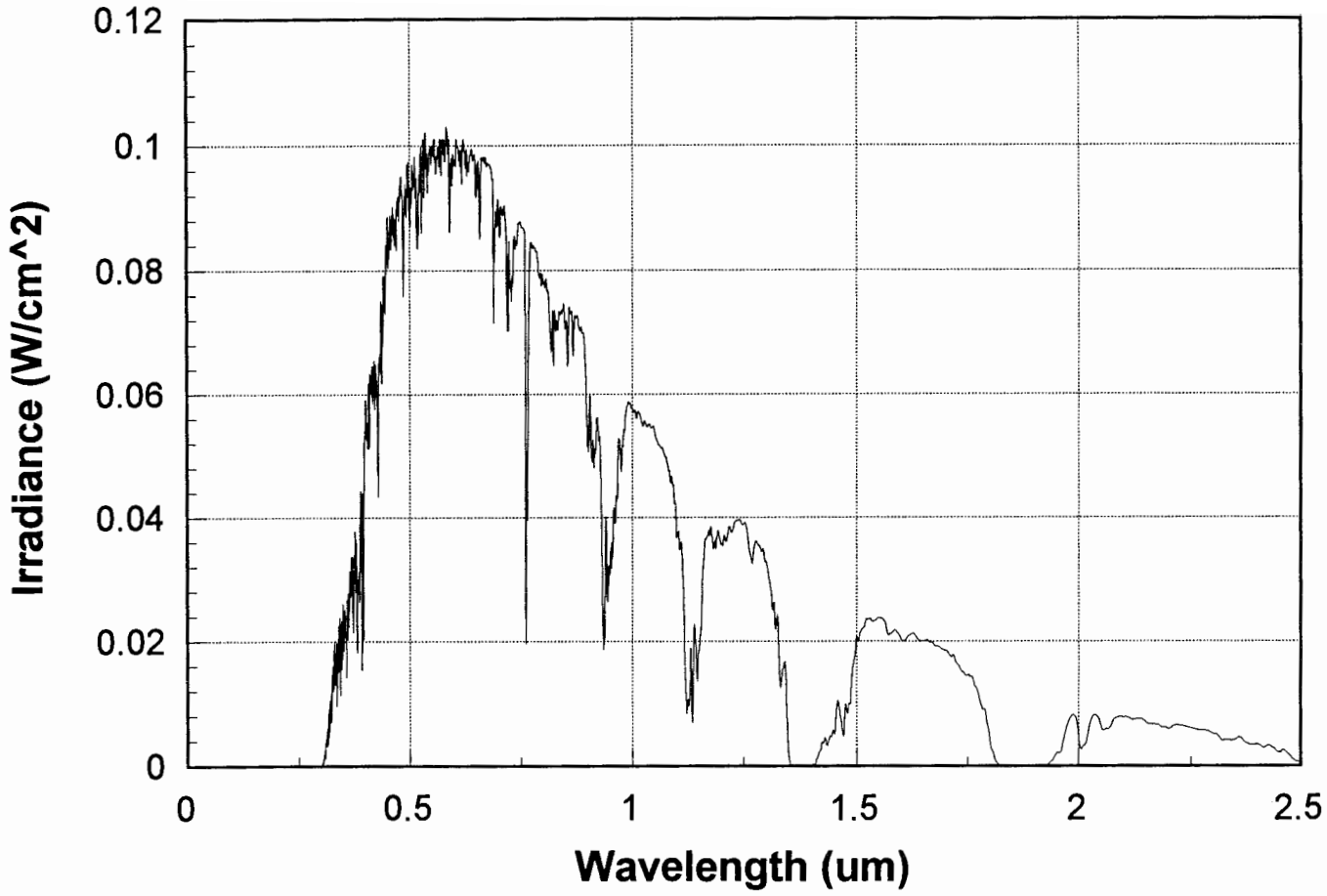

Figure 5.6. Solar Irradiance at sea level as modelled by Lowtran 7 assuming 5 km visibility

the signal area.

Another technique for avoiding day-sky background is to operate at in the solar blind region (230-300 nm), where ozone absorption in the atmosphere attenuates the solar radiance. This technique has not had wide spread use because the attenuation also limits the lidar signal, limiting the sensing range.

Chapter 6

Results

6.1 Total Optical Efficiency

The total optical efficiency of the scanning lidar system, η_{eff}, can be expressed as the product of the subsystem efficiencies,

$$\eta_{eff} = \eta_{transmitter}\,\eta_{receiver}\,\eta_{fiber}\,\eta_{detector} \qquad (6.1)$$

Table 6.1 summarizes the subsystem efficiencies determined in the previous chapters and gives the total optical efficiency of the system.

Table 6.1. Total Optical Efficiency

Optical Efficiency	**355 nm Channel**	**532 nm Channel**	**607 nm Channel**	**1064 nm Channel**
Transmitter	0.38	0.79	(0.79)	0.83
Receiver				
P-polarization	0.67	0.67	0.64	0.71
S-polarization	0.51	0.50	0.49	0.54
Fiber Coupler	0.62	0.90	0.90	0.89
Detector	0.11	0.14	0.25	0.087
Total Efficiency				
P-polarization	**0.018**	**0.067**	**0.11**	**0.045**
S-polarization	**0.014**	**0.051**	**0.088**	**0.035**

Table 6.1 shows that the optical efficiency is dependent primarily upon wavelength and polarization, $\eta(\lambda,\Theta_{pol})$. To be accurate, the efficiency is also dependent upon range, temperature, degree of misalignment, and other factors. These other factors are undesirable and are kept as minimal, or constant, as possible.

6.2 Expected Photon Return

Recalling the lidar equation (Eq. 1.2), it is now possible to model expected photon return for the LARS scanning lidar system. However, a few system parameters still need to be determined.

6.2.1 Atmospheric Transmission, T(λ,R)

Atmospheric transmission must be integrated along the laser path to account for extinction of the optical signal from absorption and scattering. The transmission factor can be calculated using the Beer-Lambert law,

$$T(\lambda,R) \equiv e^{-\int_0^R \kappa(\lambda,R)\,dR} \tag{6.2}$$

where $\kappa(\lambda,R)$ is the atmospheric attenuation coefficient.

A model of atmospheric transmission was generated with LOWTRAN 7, and is shown in Figure 6.1.

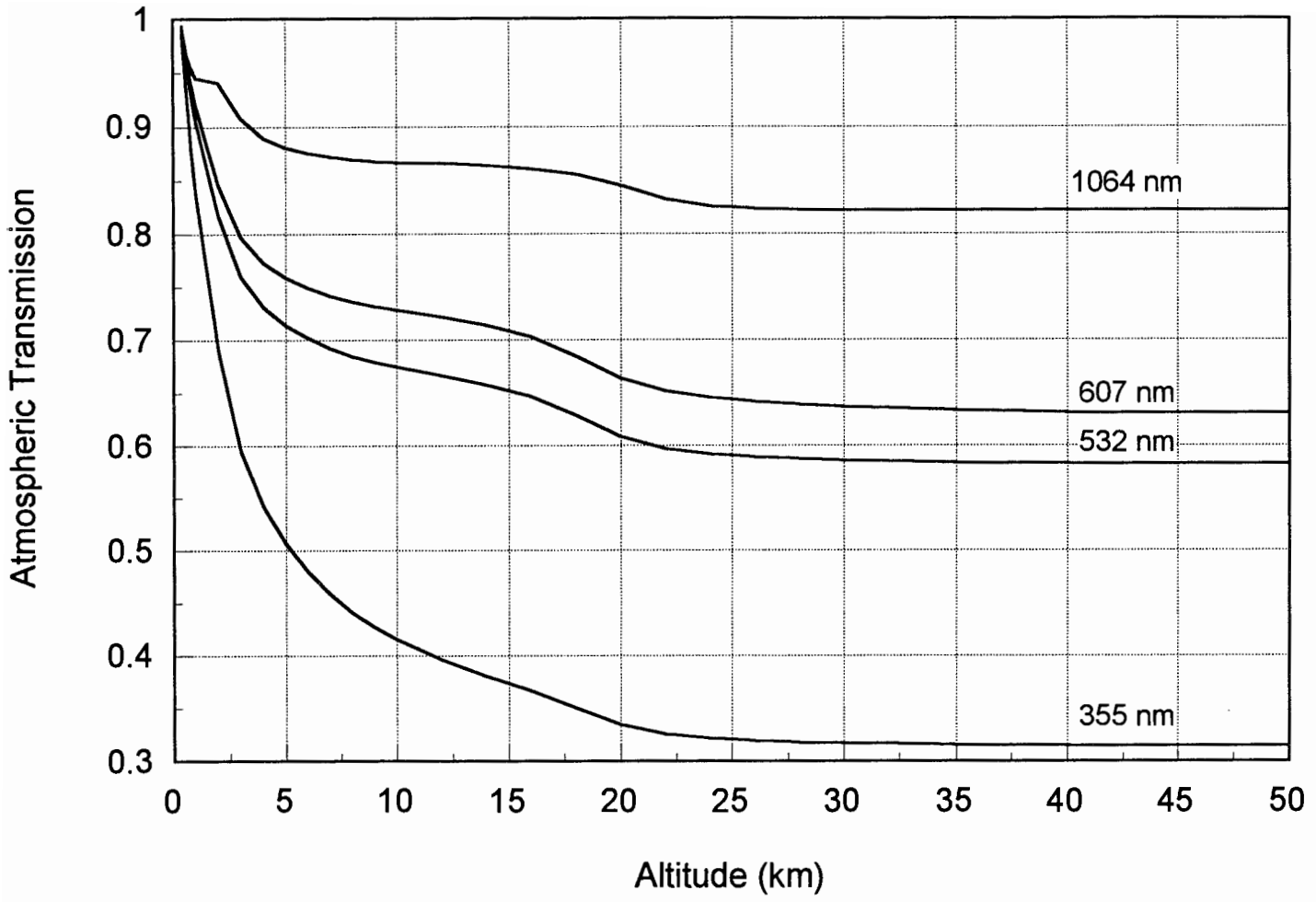

Figure 6.1. Atmospheric transmission profiles modelled with Lowtran 7

6.2.2 Backscattering Cross-section Coefficient

Details of how to calculate the molecular Rayleigh backscattering coefficients are discussed by Measures (1992, pp.38-47). For Rayleigh scattering, the backscattering cross-section of the atmosphere below 100 km can be approximated with,

$$\sigma_{\pi}^{R}(\lambda) = 5.45[\frac{550}{\lambda(nm)}]^{4} \times 10^{-28}\ cm^{2}\,sr^{-1} \quad . \qquad \textbf{(6.3)}$$

The backscattering coefficients for the LARS wavelengths are,

σ_{π}^{Ray} (355 nm) = 31.4 x 10^{-28} cm^2 sr^{-1},

σ_{π}^{Ray} (532 nm) = 6.22 x 10^{-28} cm^2 sr^{-1},

σ_{π}^{Ram} (607 nm) = 0.00564 x 10^{-28} cm^2 sr^{-1},

σ_{π}^{Ray} (355 nm) = 0.389 x 10^{-28} cm^2 sr^{-1}.

6.2.3 Atmospheric Number Density

Values for atmospheric number density are taken from the US Standard Atmosphere 1976 (p. 15). The US Standard Atmosphere 1976 is a model of the atmosphere resulting from a multitude of experimental measurements and theoretical computations. Figure 6.2 shows the atmospheric number density from the U.S. Standard model. Because nitrogen is uniformly mixed in a dry atmosphere, the nitrogen number density can be calculated by multiplying the atmospheric number density by 0.78.

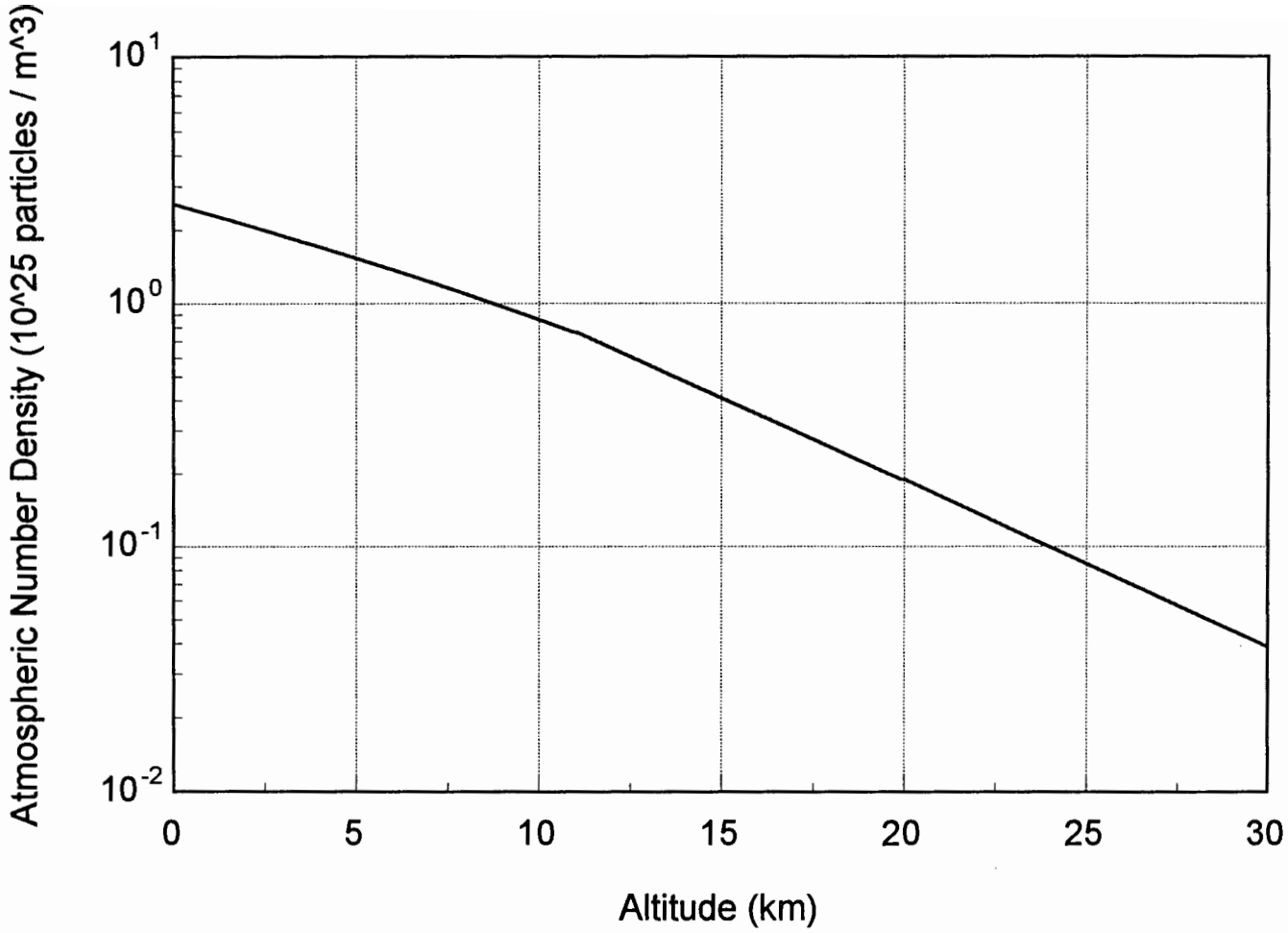

Figure 6.2. Atmospheric Number Density from the U.S. Standard Atmosphere 1976 (p. 15)

6.2.4. Photon Return

Figure 6.3 shows a profile of the expected photon return for the LARS system for each wavelength. Unfortunately, this model could not be compared to an experimental measurement because the system is not fully operational yet. It is expected that the actual photon returns will be slightly less than modelled due to small misalignments of the optical components, especially the coupling fiber.

6.3 Suggestions for Improvement

Previous measurement experiences with the LAMP lidar system allowed for LARS to be designed with many improvements. However, there are still enhancements to the system that would improve system performance.

The size of the laser and telescope were limited by the conditions that they be compact and lightweight for mounting on the scanning platform. Thus, extra sensitivity can not be achieve by going to a higher powered laser or a larger area telescope. The total transmittance of the optical system must be as high as possible to achieve the best sensitivity. To improve the optical efficiency, the uncoated optics could be anti-reflection (AR) coated. Surface reflection is the primary loss mechanism for the lenses and windows in the transmitter and receiver systems. AR-coating is wavelength dependent; it can not eliminate all reflection, but an increase of a few percent in transmission for each optical component would result in a significant improvement overall.

A significant amount of power was lost even before the laser beams (three wavelengths) were emitted into the atmosphere. To steer the transmitter beams through the

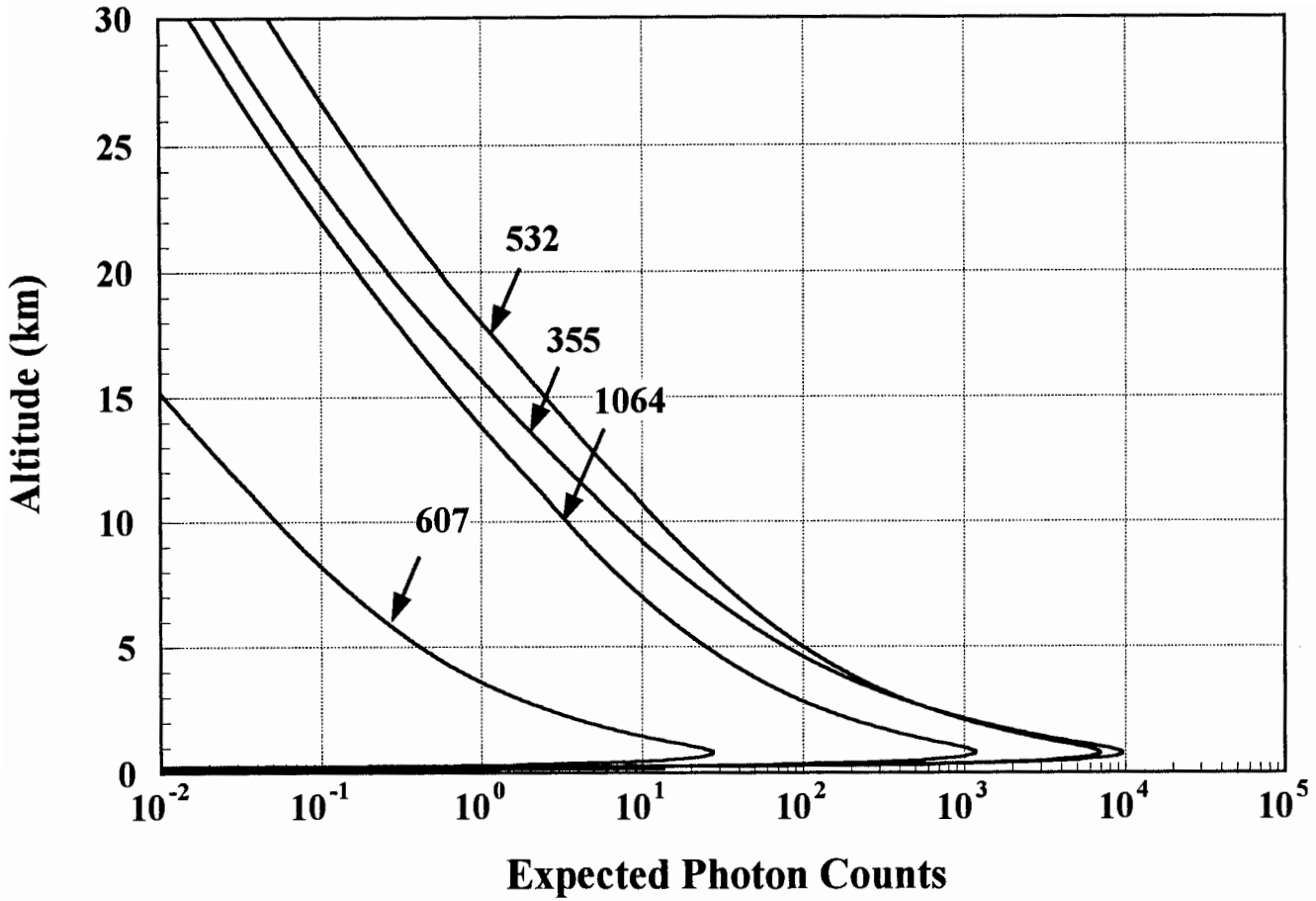

Figure 6.3. Expected photon return for each LARS channel for 1s accumulation (20 laser pulses)

beam expander and into alignment with the telescope, four laser hard-coated mirrors were used. For reflection at an angle a mirror will always be more efficient at reflecting the perpendicular polarization. Since the laser beams are steered through two different orthogonal planes, the beams will reflect from two mirrors with perpendicular polarization and two with parallel polarization. Using a waveplate to rotate the laser beams, the transmitter system can be made more efficient.

Stability of the optical efficiency of the transmitter/receiver/detector system is the most significant, *controllable* source of noise in the lidar system. For the narrrowband interference filters, small temperature variations can cause large changes in transmission. To improve stability, the filters should have a small thermal coefficient. Metal oxide filters are available that have lower thermal coefficients than dielectric fluoride filters used in the visible-infrared region (metal oxide was used for the ultraviolet filter because that is all that is available). However, there is a trade-off between cost and efficiency because the metal oxide filters are much more expensive than the fluoride filters.

Chapter 7

Conclusions

Performance efficiencies have been evaluated for each subsystem of the LARS scanning lidar system through a combination of experimental efficiency measurements and theoretical calculations. Combining these results for a total system efficiency, a model of expected photon was presented. It is expected that the actual photon return will be consistent with the system model. Large deviations of experimental measurements from the performance model can indicate that there is a problem with system, and that the alignment needs to be adjusted.

In the analysis of each subsystem, possible sources of poor efficiency were discussed. Variations in optical efficiency due to the sensitivity of narrowband filters and dichroic beamsplitters to temperature and angle of incidence were discussed and methods of reducing the variation were mentioned. Characteristics that caused system bias, such as fiber propagation delay, photomultiplier tube transit time, and dark current were determined. Other noise sources such as shot noise, thermal noise, and efficiency noise (changes in efficiency from various effects) decrease the signal-to-noise of the system and limit the sensitivity of the system. Characterizing these noise sources allowed for improvements to the system to be suggested.

References

F. C. Allard, *Fiber Optics Handbook: For Engineers and Scientists*. New York: McGraw-Hill Publishing Co., 1990.

Andover Corporation, *Optical Filter Guide*, New Hampshire, 1992.

C.F. Bohren and D. R. Huffman, *Absorption and Scattering of Light by Small Particles.* New York: John Weley & Sons, 1983.

A. I. Carswell, "Lidar Remote Sensing of Atmospheric Aerosols," SPIE vol. 1312, Propagation Eng., 206-220, 1990.

C. E. Clark and K.T. Whitby, "Concentration and Size Distribution Measurements of Atmospheric Aerosols and a Test of the Thoeory of Self-Preserving Size Distributions," J. of Atm. Sciences, vol. 24, 677-686, 1967.

D.P. Donovan, J.A. Whiteway, and A.I. Carswell, "Correction for Nonlinear Photon-counting Effects in Lidar Systems," Applied Optics, vol. 32, no. 33, 6742-6753, 1993.

G. Fiocco and L.D. Smullin, "Detection of Scattering Layers in the Upper Atmosphere (60-140 km) by Optical Radar," Nature (London), vol. 199, no. 4900, 1275-1276, 1963.

P.A.T. Harris, "Performance Analysis of the Lamp Rayleigh/Raman Lidar System," MS Thesis, The Pennsylvania State University, 1992.

R. M. Measures, *Laser Remote Sensing*. Florida: Krieger Publishing Co., 1992.

C.R. Philbrick, D.B. Lysak, Y.-C. Rau, "Lidar Measurements of Aerosol Scattering in the Troposphere and Stratosphere," COMEAS Proceedings, 107-110, 1993.

S. Rajan, G. R. Evanisko, T.J. Kane, C.R. Philbrick, "Aerosol Mapping of the Atmosphere Using a Multiple Wavelength Polarization Lidar," COMEAS Proceedings, 111-114, 1993.

Thorn EMI Electron Tubes, Ltd., *Photomultipliers and Accessories*, New Jersey, 1993.

H. Rutten and M. van Venrooij, *Telescope Optics: Evaluation and Design*. Virginia: Willmann-Bell, 1988.

K. Sassen, "The Polarization Lidar Technique for Cloud Research: A Review and Current Assessment," Bull. of the Amer. Meteo. Soc., vol. 72, no. 12, 1848-1866, 1991.

C.Y. She, R.J. Alvarez II, L.M. Caldwell, D.A. Kruegger, "High-spectral-resolution Rayleigh-Mie lidar measurement of aerosol and atmospheric profiles," Optics Letters, vol. 17, no. 7, 541-543, 1992.

S.T. Shipley, D.H. Tracy, E.W. Eloranta, et al., "High spectral resolution lidar to measure optical scattering properties of atmospheric aerosols. 1: Thoeory and Instrumentation," Applied Optics, vol. 22, no. 23, 3716-3724, 1983.

J.D. Sphinhirne, J.A. Reagam, B.M. Herman, "Vertical Distribution of Aerosol Extinction Cross Section and Inference of Aerosol Imaginary Index in the Troposphere by Lidar Technique," J. of App. Meteo., vol. 19, 426-438, 1980.

U.S. Standard Atmosphere, 1976, National Oceanic and Atmospheric Administration, Washington, D.C., 1976.

A. Yariv, *Optical Electronics*, 4 ed. Philadelphia.: Saunders College Publishing, 1991.

Appendix

Optical Spectra of LARS Components

*All spectra in this appendix were measured on a

Hitachi U-4001 Recording Spectrophotometer

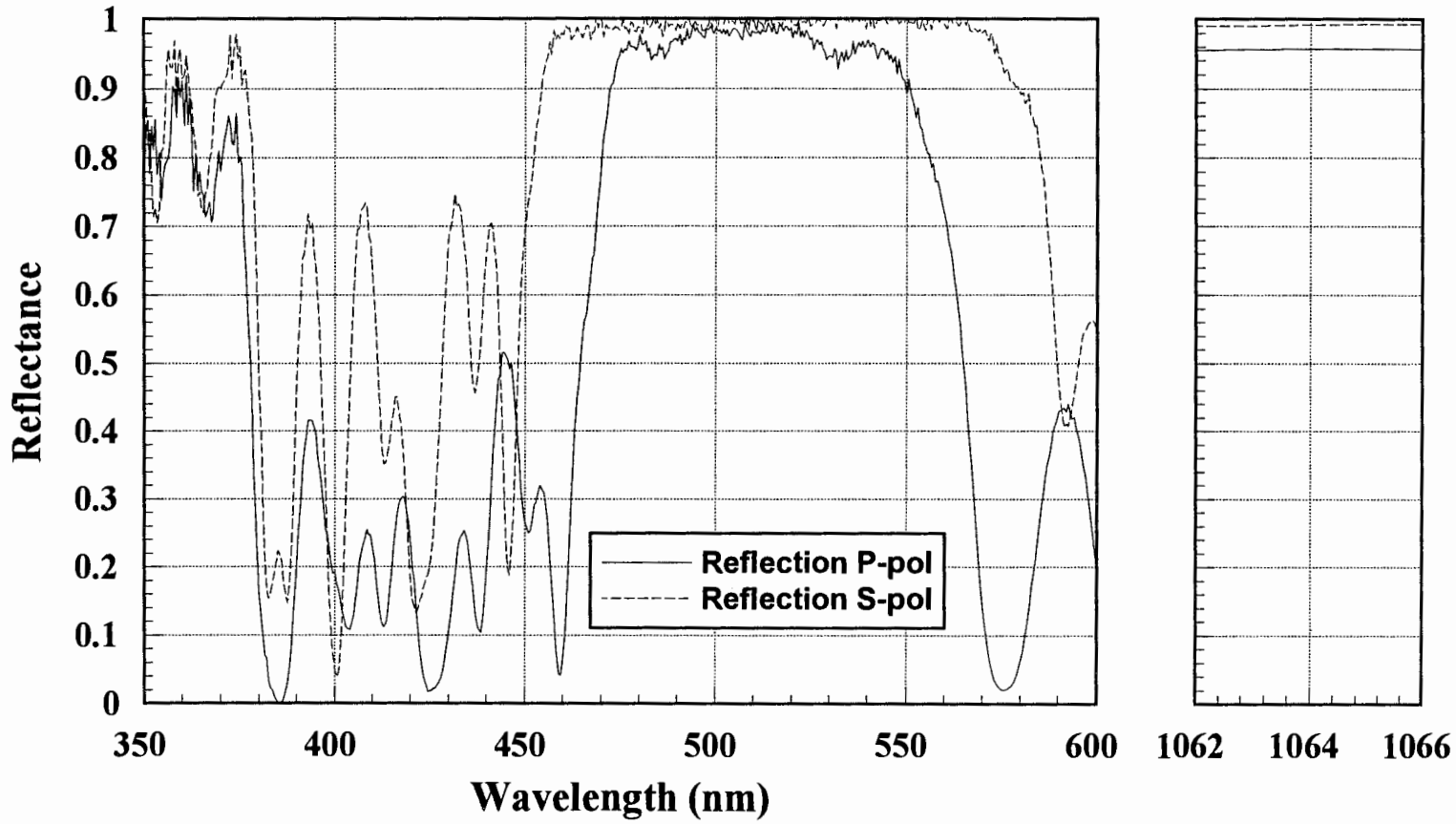

Figure A.1. Reflectance at 45 degrees for the transmitter beamsteering mirors

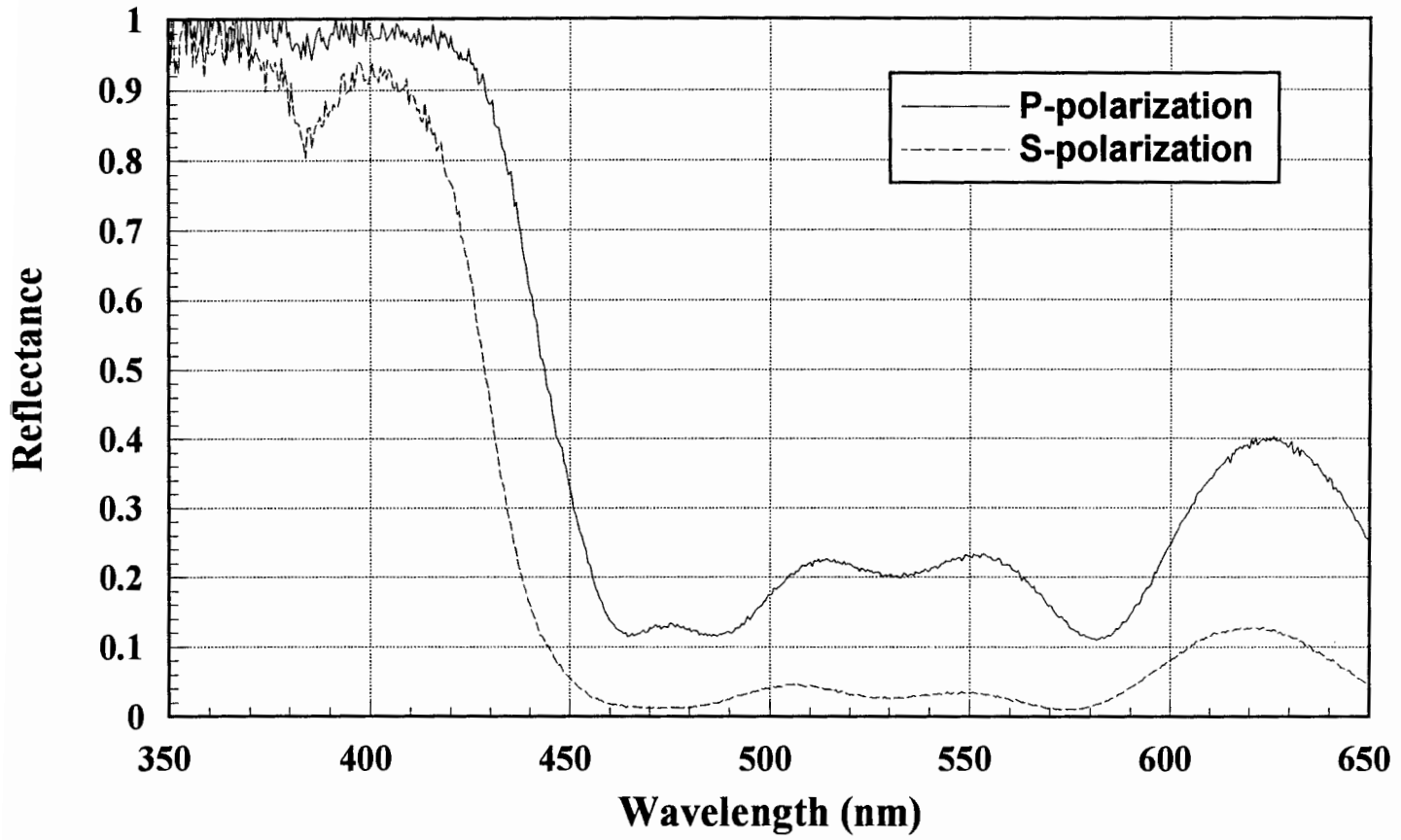

Figure A.2. Reflectance at 45 degrees for the 355 nm beamsplitters

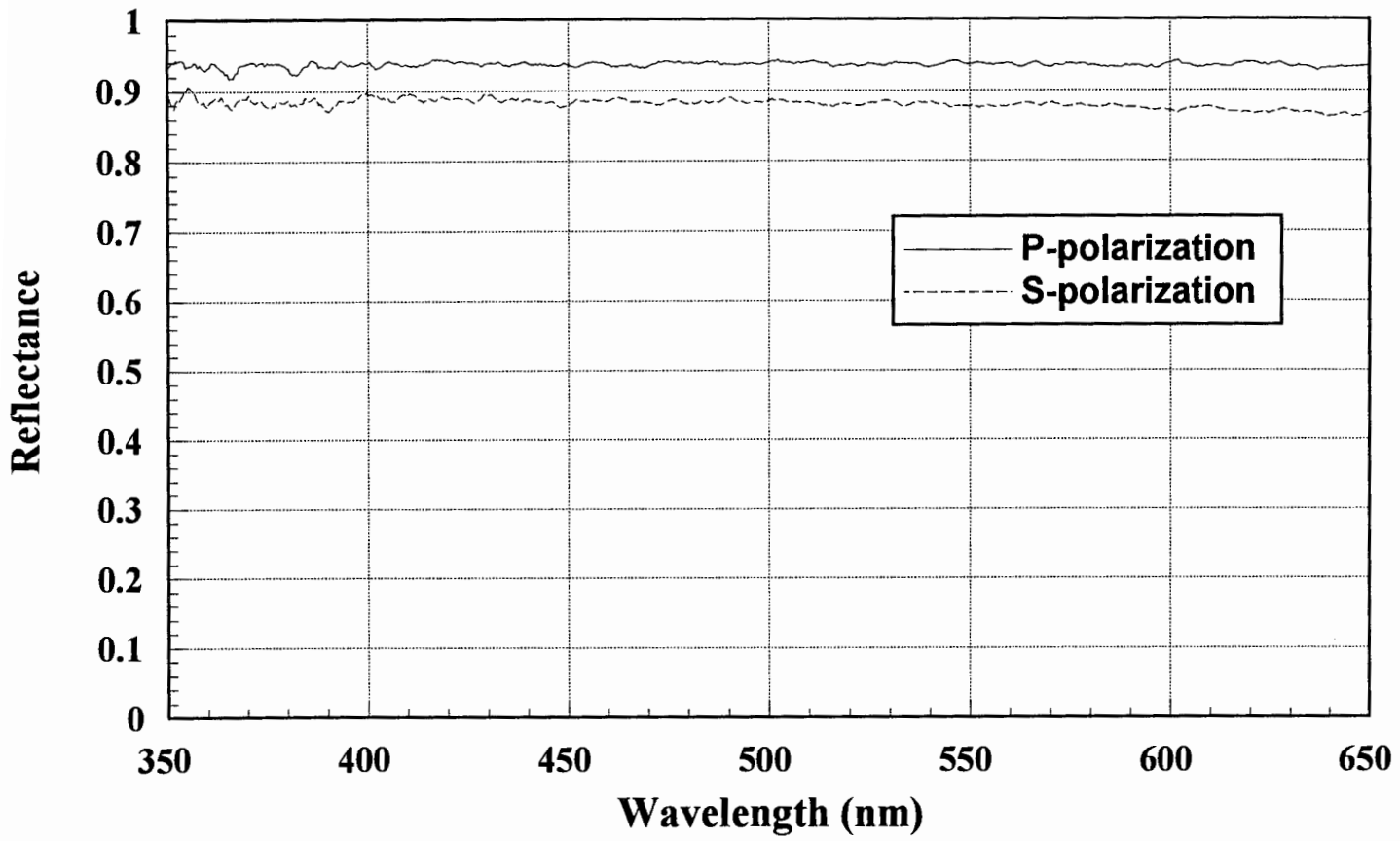

Figure A.3. Reflectance at 45 degrees for the broadband mirror (532 nm channel)

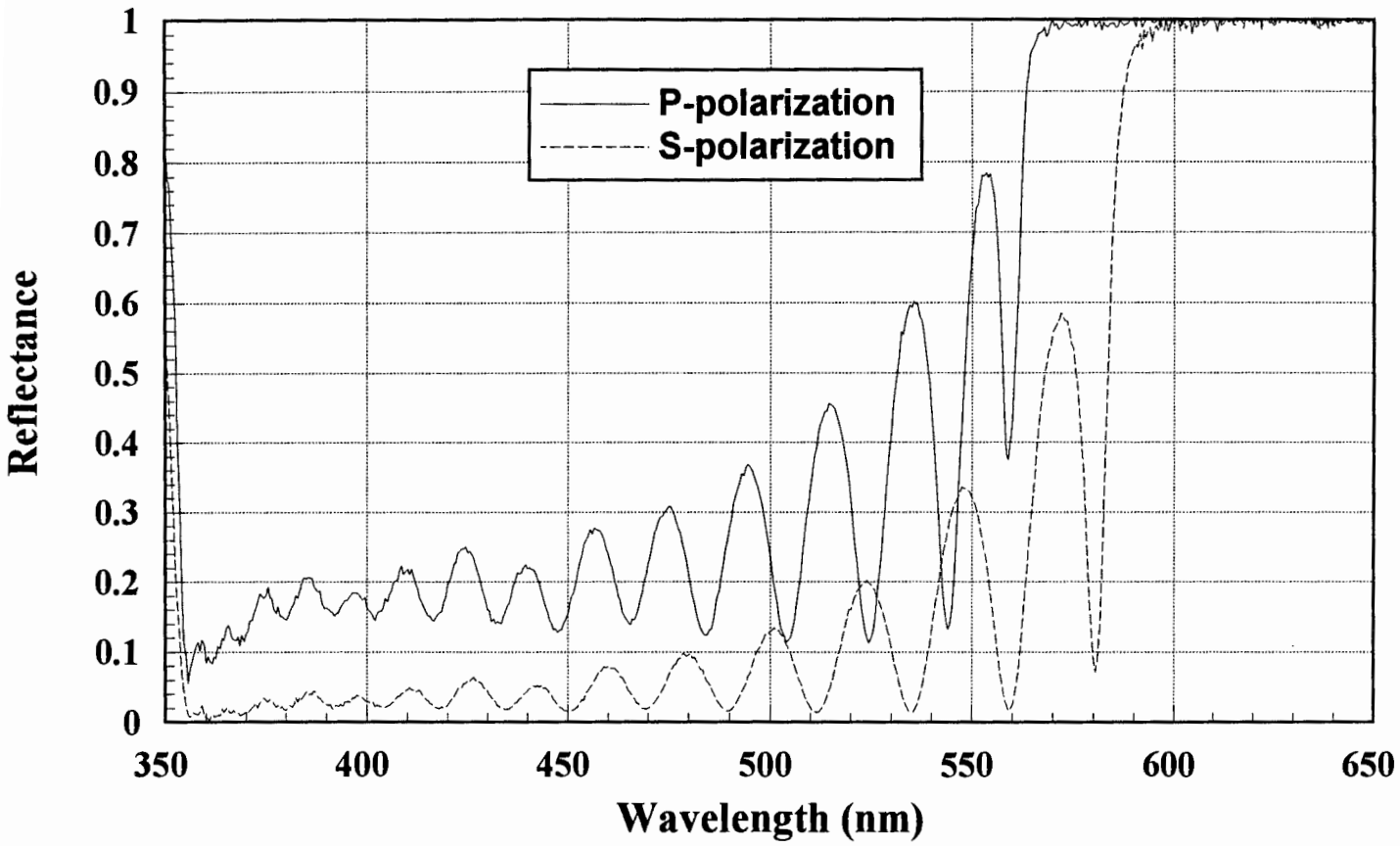

Figure A.4. Reflectance at 45 degrees for the 607 nm beamsplitters

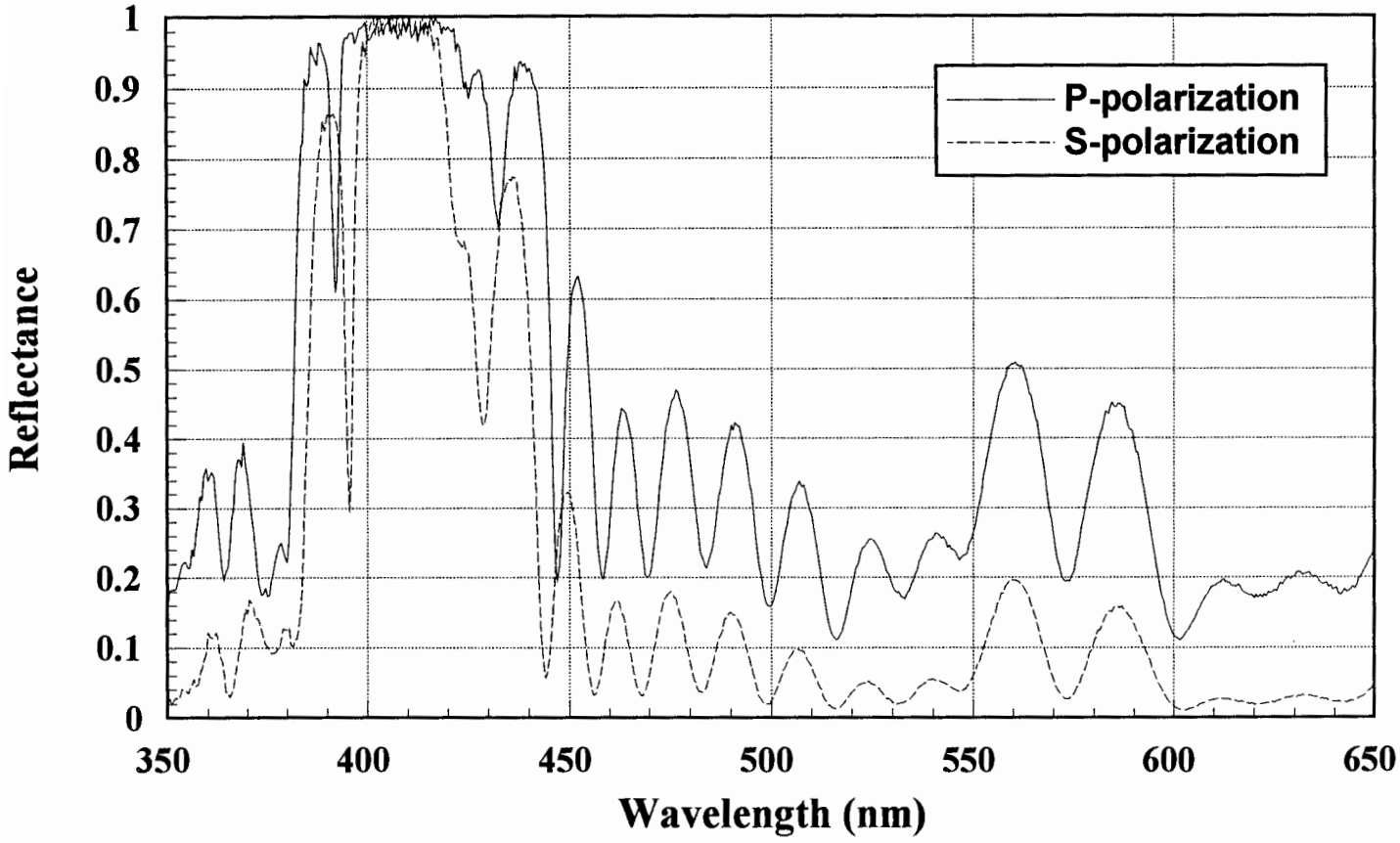

Figure A.5. Reflectance at 45 degrees for the 1064 nm beamsplitters

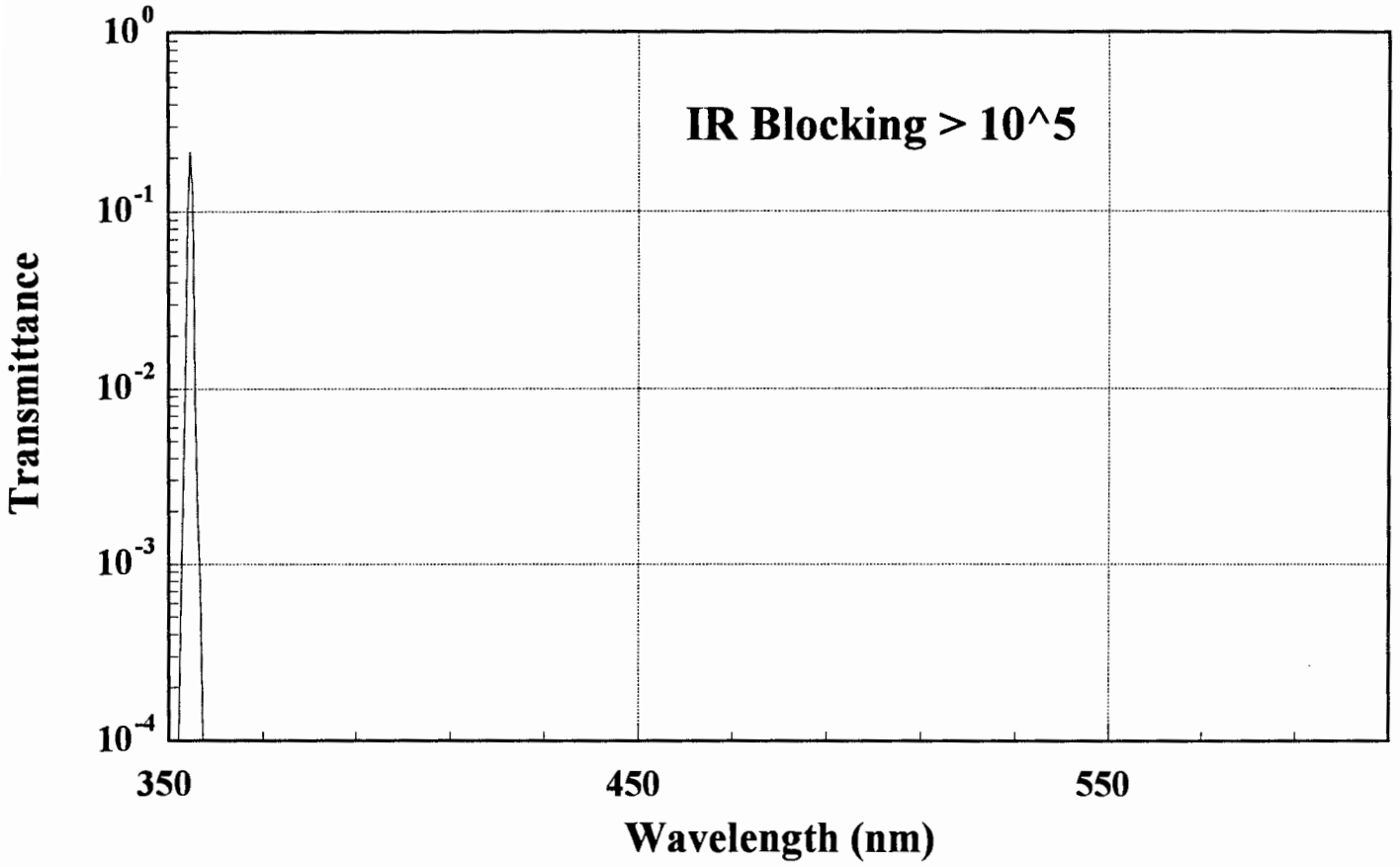

Figure A.6. 355 nm narrow band filter transmittance

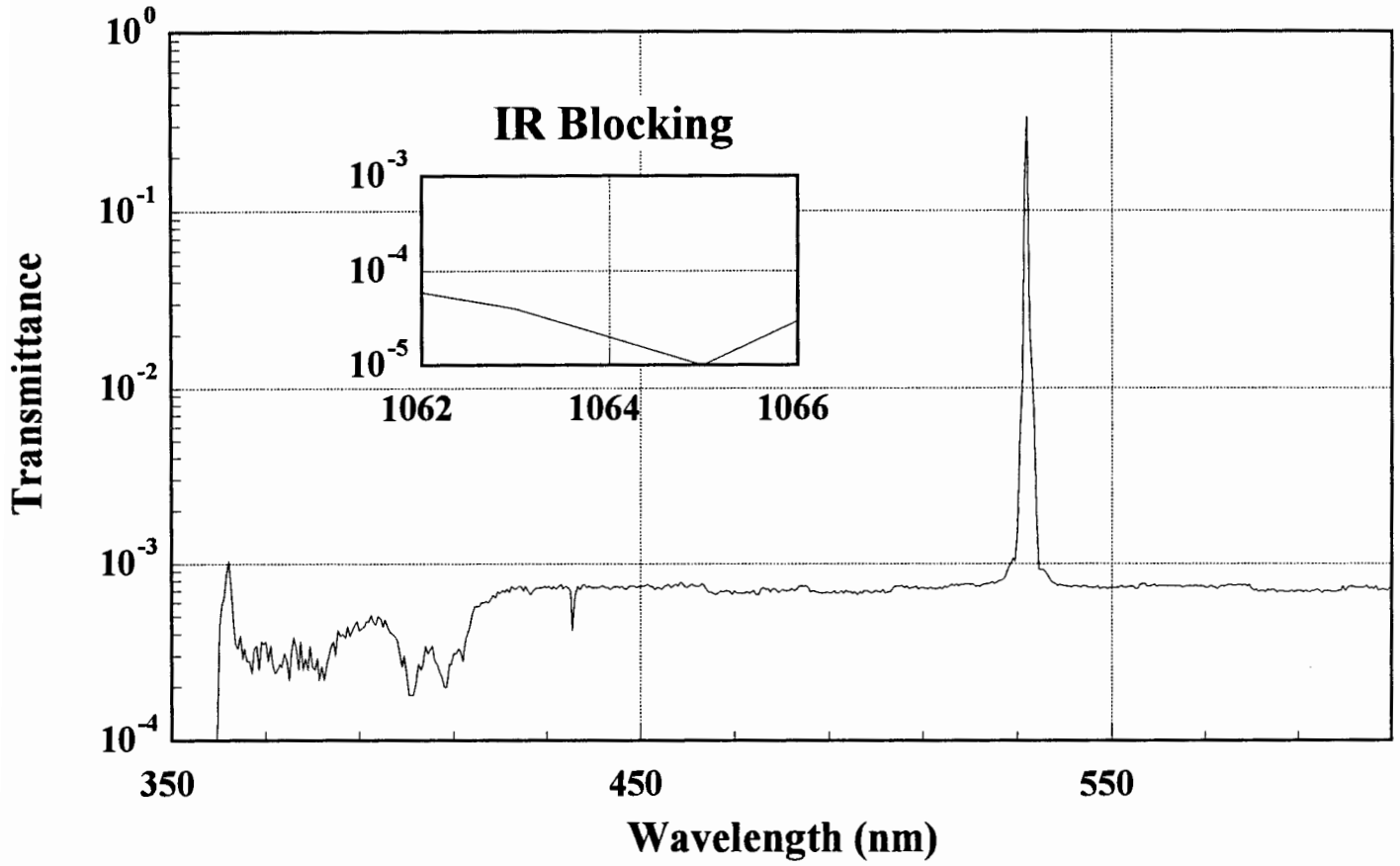

Figure A.7. 532 nm narrow band filter transmittance

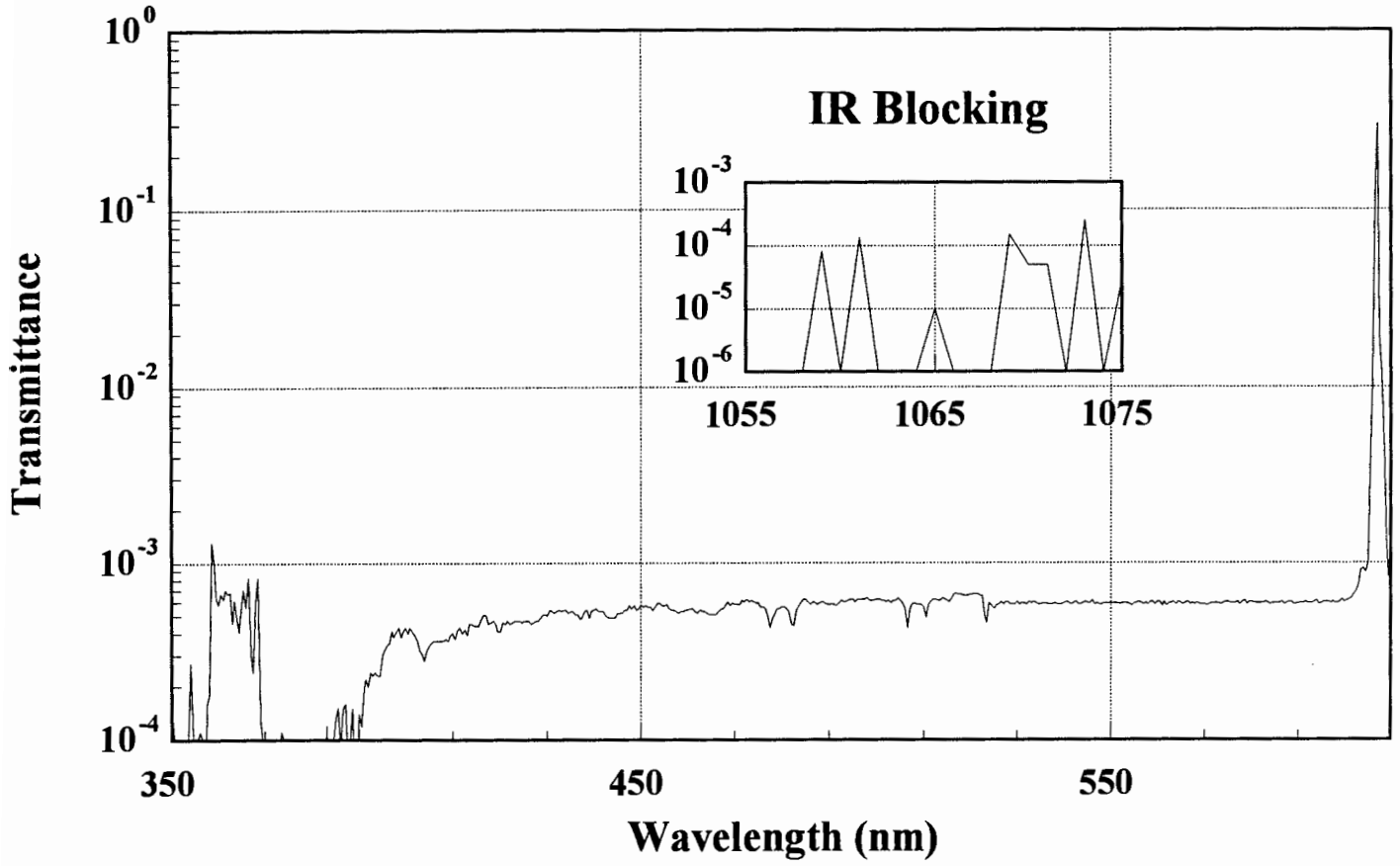

Figure A.8. 607 nm narrow band filter transmittance

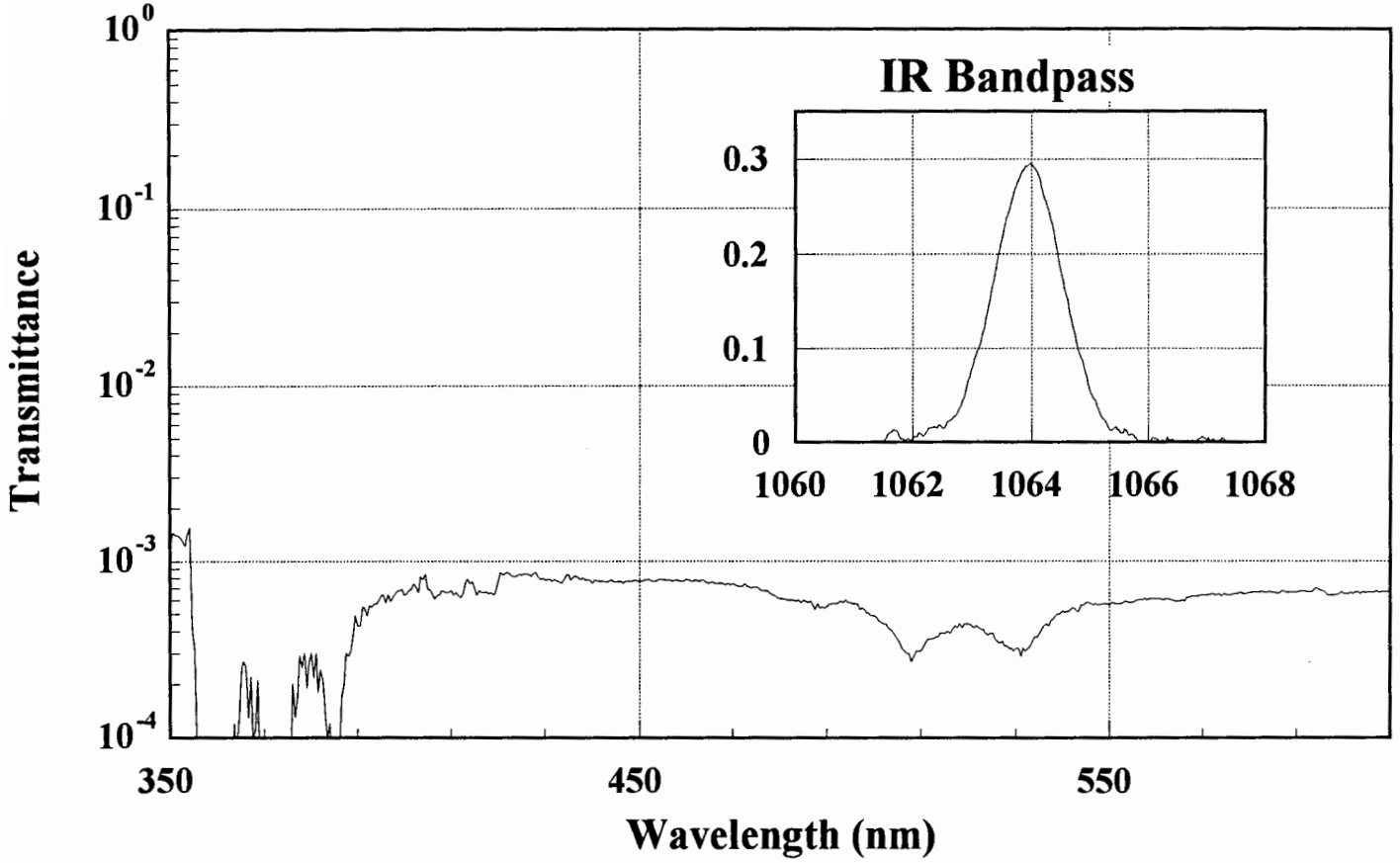

Figure A.9. 1064 nm narrow band filter transmittance

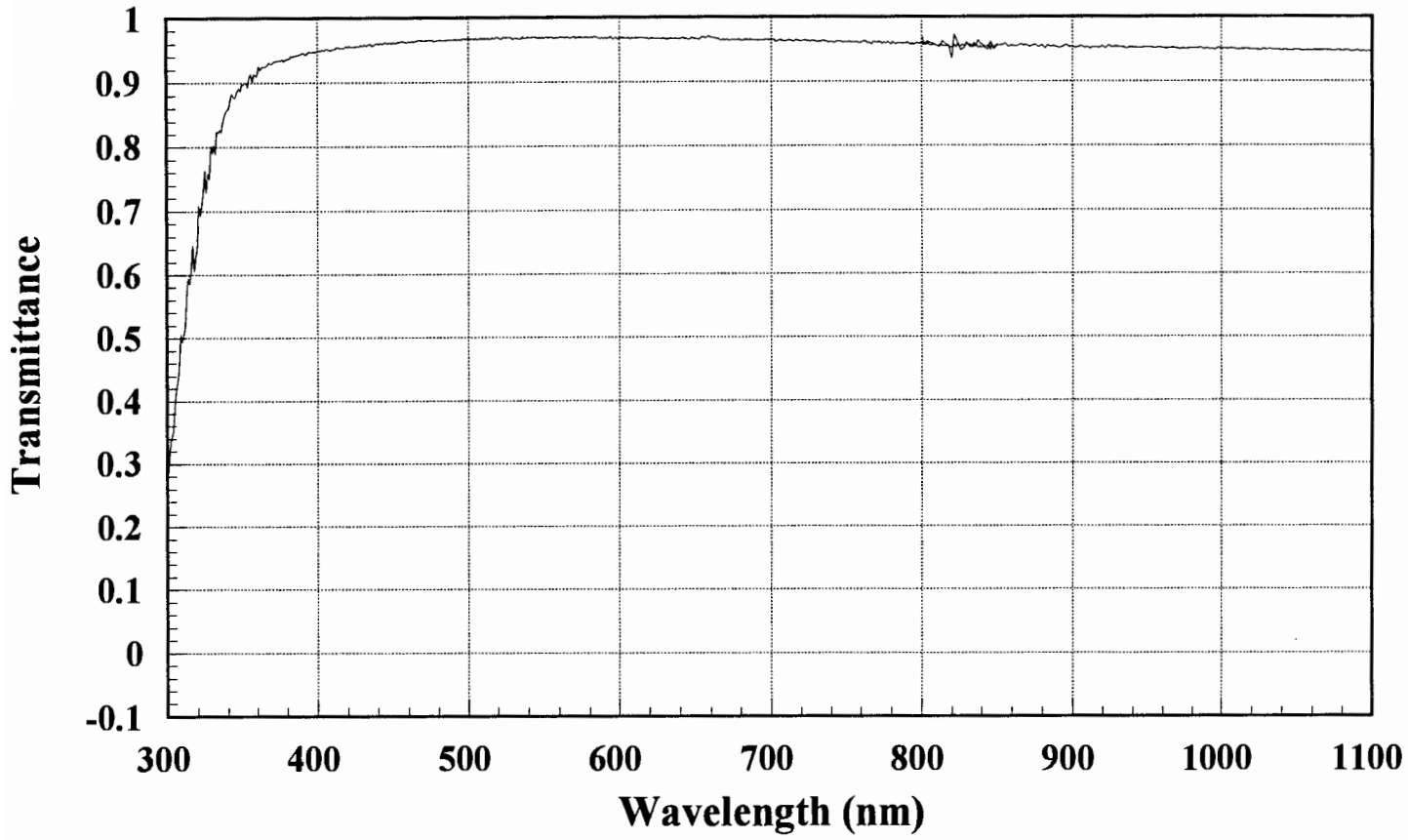

Figure A.10. BK7 Window Transmittance